ELSEVIER

Advances in Colloid and Interface Science 118 (2005) 1 – 24

ADVANCES IN COLLOID AND INTERFACE SCIENCE

www.elsevier.com/locate/cis

Application of the extended RSA models in studies of particle deposition at partially covered surfaces

Paweł Weroński

Theoretical Division and Center for Nonlinear Studies, Los Alamos National Laboratory, Los Alamos, NM 87545, USA
Institute of Catalysis and Surface Chemistry, Polish Academy of Sciences, ul.Niezapominajek 8, 30-239 Kraków, Poland

Available online 8 August 2005

Abstract

This paper reviews the application of the extended random sequential adsorption (RSA) approaches to the modeling of colloid-particle deposition (irreversible adsorption) on surfaces precovered with smaller particles. Hard (noninteracting) particle systems are discussed first. We report on the numerical simulations we performed to determine the available surface function, jamming coverage, and pair-correlation function of the larger particles. We demonstrate the effect of the particle size ratio and the small particle surface coverage. We found that the numerical results were in reasonable agreement with the formula stemming from the scaled-particle theory in 2D with a modification for the sphere geometry. Next, we discuss three approximate models of adsorption allowing electrostatic interaction of colloid particles at a charged interface, employing a many-body superposition approximation. We describe two approaches of the effective hard-particle approximation next. We demonstrate the application of the effective hard-particle concept to the bimodal systems and present the effect of electrolyte concentration on the effective particle size ratio. We present the numerical results obtained from the theoretical models of soft-particle adsorption at precovered surfaces. We used the effective hard-particle approximation to determine the corresponding simpler systems of particles, namely the system of hard spheres and the system of hard discs at equilibrium. We performed numerical computations to determine the effective minimum particle surface-to-surface distance, available surface function, jamming coverage, and pair-correlation function of the larger particles at various electrolyte ionic strengths and particle size ratios. The numerical results obtained in the low-surface coverage limit were in good agreement with the formula stemming from the scaled-particle theory with a modification for the sphere geometry and electrostatic interaction. We compared the results of numerical computations of the effective minimum particle surface-to-surface distance obtained using the 2D, 3D, and curvilinear trajectory model. The results obtained with the 3D and curvilinear trajectory models indicate that large-particle/substrate attractive interaction significantly reduces the kinetic barrier to large, charged-particle adsorption at a surface precovered with small, like-charged particles. The available surface function and jamming-coverage values predicted using the simplified 3D and the more sophisticated curvilinear trajectory models are similar, while the results obtained with the 2D model differ significantly. The pair-correlation function suggests different structures of monolayers obtained with the three models. Unlike the three models of the electrostatic interaction, both effective hard-particle approximations give almost identical results. Results of this research clearly suggest that the extended RSA approaches can fruitfully be exploited for numerical simulations of colloid-particle adsorption at precovered surfaces, allowing the investigation of both hard and soft-particle systems.
Published by Elsevier B.V.

Keywords: Adsorption of colloid particles; Particle electrostatic interaction; Colloid deposition; Monte Carlo simulation; Random sequential adsorption; RSA model

Contents

1. Introduction 2
2. Hard-particle systems 3

E-mail address: pawel@cnls.lanl.gov.

0001-8686/$ - see front matter. Published by Elsevier B.V.
doi:10.1016/j.cis.2005.03.002

2.1. The simulation algorithm . . . 3
2.2. Analytical approximation . . . 4
2.3. Results of computation . . . 5
2.3.1. Available surface function . . . 5
2.3.2. Maximum surface coverage . . . 6
2.3.3. Pair-correlation function . . . 7
3. The electrostatic interaction models . . . 9
3.1. 2D model . . . 9
3.2. 3D model . . . 9
3.3. CT model . . . 10
4. The effective hard-particle approach . . . 11
4.1. Monodisperse systems . . . 11
4.2. Extension of the EHP approach to the bimodal systems . . . 12
5. Soft-particle systems . . . 13
5.1. The simulation algorithm . . . 13
5.2. Analytical approximation . . . 14
5.3. Results of computation . . . 14
5.3.1. Effective minimum particle surface-to-surface distance . . . 15
5.3.2. Available surface function . . . 17
5.3.3. Maximum surface coverage . . . 20
5.3.4. Pair-correlation function . . . 21
6. Conclusion . . . 23
Acknowledgements . . . 24
References . . . 24

1. Introduction

The adsorption and deposition (irreversible adsorption) of colloids and bioparticles at solid/liquid interfaces are of great significance in many natural and practical processes such as water and wastewater filtration, membrane filtration, papermaking, flotation, protein and cell separation, enzyme immobilization, biofouling of membranes, and artificial organs. Often in these processes, especially in filtration, polydisperse suspensions or mixtures appear, e.g., colloid/polymer, colloid/macroscopic particle, or protein/surfactant. As a result of their higher diffusivity, the smaller components of the mixture will adsorb preferentially at the interface, forming a layer that may prohibit consecutive deposition of larger particles. This effect leads to a considerable decrease in the kinetics of large-particle accumulation at the interface as reported in the literature [1–3]. Similar problems often appear in model experiments concerned with protein or colloid-particle adsorption when the usual substrate cleaning procedure may produce a nanosized contaminant layer difficult to detect by conventional means. Formation of such a layer will produce surface heterogeneity, in respect to both charge distribution and geometry, which is expected to influence the kinetics and maximum coverage of the adsorption experiments. Thus, modeling of adsorption phenomena at precovered surfaces seems an important and challenging task that can be accomplished using a variety of approaches. Among them, the random sequential adsorption (RSA) approach seems to be the most suitable because of its simplicity and efficiency.

The classical RSA model considers a sequence of trials of particle adsorption at a homogeneous interface [4–6]. Once an empty surface element is found, the particle is permanently fixed with no consecutive motion allowed. Otherwise, the virtual particle is rejected and a next-addition attempt is undertaken. Since 1980s a number of extended RSA models have been developed that include the effects of particle shape [7–11], Brownian motion [12–15], external force [16–19], particle–particle [20–22] and particle–interface [23] electrostatic interaction, colloid-particle polydispersity [24–26], and surface heterogeneity [27–30]. The results based on RSA simulations allow us to predict particle monolayer structure and the jamming coverage of particles. We can use the model to predict particle-adsorption kinetics as well, although, depending on the particle-transport mechanism, an appropriate analysis of real adsorption problems can require including a correction for bulk transport or the hydrodynamic scattering effect [31]. Thus, RSA modeling can be a powerful tool in the study of irreversible adsorption of macromolecules, proteins, and colloid particles.

The goal of this paper is to present a short review of methods used and preliminary results obtained in RSA numerical simulations of colloid adsorption at precovered surfaces. Many of these results have been published in Refs. [3,27,28,32–34]. First, we present the simulation algorithms for hard and soft particles. Next, we discuss the existing 2D, 3D, and curvilinear trajectory (CT) models of particle adsorption including the electrostatic interaction at the adsorption surface. We follow by demonstrating the application of the effective hard-particle (EHP) approach to the bimodal system of particles. Our determination of the available surface function (ASF), jamming coverage, radial distribution function, and effective minimum particle

surface-to-surface distance are presented next. Lastly, we verify the effect of the particle size ratio, small-particle surface coverage, and electrolyte ionic strength on the characteristics of the adsorption process.

2. Hard-particle systems

Let us assume that repulsive (interparticle) interactions in our system are of the hard-particle type, i.e., the net interaction energy tends to infinity when the particles overlap and to zero otherwise. We also assume localized adsorption of the particles, which means that no consecutive motion of the adsorbed particles is allowed. Experimentally, the system can be realized at high ionic strength if the small and large particles bear the same surface charge. We can produce a random surface by covering a homogeneous interface with N_s small spherical particles of radius a_s. (In what follows, the subscripts s and l will always refer to small and large particles, respectively.) The number of adsorbed particles can be expressed in terms of dimensionless surface coverage defined as

$$\theta_i = \pi a_i^2 N_i / S, \quad i = \mathrm{s,l}, \tag{1}$$

where S is the geometrical area of the interface. The particle distribution is known a priori and can quantitatively be characterized in terms of the pair-correlation function (called also radial distribution function) defined as

$$g_i(\mathbf{r}) = \frac{S}{N_i^2}\left\langle \sum_{j=1}^{N_i}\sum_{m=1}^{N_i} \delta\left[\mathbf{r} - \left(\mathbf{r}_m - \mathbf{r}_j\right)\right]\right\rangle, \quad i = \mathrm{s,l}, \tag{2}$$

where $\mathbf{r}$ is the position vector of a point over the adsorption plane (measured from the center of an adsorbed particle), δ is the Dirac delta function, $\mathbf{r}_j$ and $\mathbf{r}_m$ are the position vectors of the particles j and m, respectively, and angle brackets mean the ensemble average. In the absence of external forces when the system can be considered as isotropic, the vector $\mathbf{r}$ can be replaced with the radial coordinate r and the pair-correlation function may be calculated more directly by converting Eq. (2) to the form

$$g_i(\mathbf{r}) = g_i(r) = \frac{S}{N_i}\frac{\hat{N}_a(r)}{2\pi r \Delta r}, \quad i = \mathrm{s,l}, \tag{3}$$

where $\hat{N}_a(r) = \langle N_a \rangle / N_i$ is the averaged number of the small or large particles within the annulus of the mean radius r and the thickness Δr.

The simplest situation arises when $g_i(r) = 1$, which corresponds to a perfectly random distribution of particles, characteristic for low surface coverage. However, when surface coverage exceeds 10%, deviations from the uniform distribution occur and particle positions become correlated, which is manifested by an increased number of pairs separated by small distances. The pair-correlation function in this case is well known from numerical simulations [20] and from experiments [20,35,36].

Now, let us consider the adsorption of larger particles (having radius a_l) at such prepared random surface. From simple geometry we can deduce that the particle can be placed at a short distance h from the surface when there are no small and large particles within the circular areas $A_i = \pi[4a_l a_i + (2a_i - 2a_l - h)h]$, $i = \mathrm{s,l}$, respectively, called the exclusion areas. Obviously, for $h = 0$, the exclusion area $A_i = 4\pi a_l a_i$, whereas for $h \geq 2a_i$ $A_i = 0$. The probability of finding such an empty area averaged over the entire surface S (which equals the probability of placing a large particle at the distance h over the interface) is defined as the ASF [5,37–39] or the surface-blocking function B_l [36,40]. This function has fundamental significance for reversible (equilibrium) systems, allowing the calculation of the thermodynamic potential of particles [37]. For the irreversible systems considered in our work, the knowledge of the blocking function is necessary for a quantitative description of particle-adsorption kinetics. Since the blocking function depends in a complicated manner on particle coverage, particle distribution, and distance h, no theoretical results have been derived yet for random surfaces. The only results, in the form of a power expansion of B_l in terms of θ_l, were formulated for a monodisperse system and homogeneous surfaces [39]. These results, discussed extensively in Ref. [40], indicate that the most significant contribution to the blocking effects comes from the region close to the interface, when the adsorbing particles approach the primary minimum distance δ_m ($h \to 0$). Within this limit, the blocking function can easily be calculated numerically for arbitrary θ_l by applying the procedure described below.

2.1. The simulation algorithm

We simulated the irreversible adsorption process using the extended RSA model, as described in Ref. [28]. The simulations were carried out over a square simulation plane with the usual periodic boundary conditions at its perimeter. The simulation plane was divided into two subsidiary grids of square areas (cells) of the size $\sqrt{2}a_s$ and $\sqrt{2}a_l$. This technique enhanced the scanning efficiency of the adsorbing-particle environment performed at each simulation step.

The entire simulation procedure consisted of two main stages. First, the simulation plane was covered with the smaller sized particles to a prescribed surface coverage θ_s. During this stage the usual RSA simulation algorithm pertinent to hard spheres was used. Then the larger spheres were adsorbed at the precovered surface by choosing at random their x_v and y_v center coordinates. At both stages the overlapping test was carried out by checking if the condition

$$(x_m - x_v)^2 + (y_m - y_v)^2 > 4a_m a_v \tag{4}$$

was met for every particle m located next to the virtual one (subscript v refers to the virtual particle). If the condition was violated for any m, the virtual particle was

rejected and a next-addition attempt was undertaken. Otherwise, the particle was permanently fixed with no consecutive motion allowed.

The algorithm enabled us to simulate adsorption kinetics in terms of the dimensionless adsorption time defined as

$$\tau = \frac{N_{\mathrm{att}}}{N_{\mathrm{ch}}}, \tag{5}$$

where N_{att} and N_{ch} are the overall and the characteristic number of the large-particle adsorption attempts, respectively. The characteristic attempt number is usually defined as $N_{\mathrm{ch}}=S/\pi a_{\mathrm{l}}^2$. The adsorption time was set to zero at the beginning of the second stage. The maximum dimensionless time attained in our simulations was 10^4, which required N_{att} of the order of 10^9. Therefore, to calculate the jamming coverage (after infinite adsorption time), the results obtained over a long time were extrapolated by using a power-law dependence. To attain sufficient accuracy, we took averages from several computer runs.

Also, we calculated the large-particle adsorption probability (blocking parameter B_{l}) using the above algorithm according to the method described by Schaaf and Talbot [5], that is, by exploiting the definition

$$B_{\mathrm{l}}(\theta_{\mathrm{s}},\theta_{\mathrm{l}}) = \frac{N^0_{\mathrm{succ}}}{N^0_{\mathrm{att}}}, \tag{6}$$

where N^0_{succ} is the number of successful adsorption events performed at fixed θ_{s} and θ_{l}. In practice, N^0_{succ} had to be about 10^5 to attain a sufficient accuracy for the ASF.

2.2. Analytical approximation

Because of a lack of appropriate expressions for the ASF in the case of the RSA of large particles at precovered surfaces, we tested the results of the simulations in terms of the equilibrium adsorption approach. This approach seems reasonable because the ASFs for the RSA and equilibrium processes are indistinguishable in the early stage of the adsorption process at low surface coverage [5].

According to the scaled-particle theory (SPT) formulated in Ref. [37] and then extended to multicomponent mixtures in Refs. [41,42], the equilibrium large-disk ASF for the bimodal suspension of disks is given by the expression

$$\begin{aligned} B_{\mathrm{ld}} &= -\ln\left(\frac{\mu^{\mathrm{R}}_{\mathrm{ld}}}{kT}\right) \\ &= (1-\theta_{\mathrm{d}})\exp\left[-\frac{3\theta_{\mathrm{ld}}+\gamma(\gamma+2)\theta_{\mathrm{sd}}}{1-\theta_{\mathrm{d}}} - \left(\frac{\theta_{\mathrm{ld}}+\gamma\theta_{\mathrm{sd}}}{1-\theta_{\mathrm{d}}}\right)^2\right], \end{aligned} \tag{7}$$

where $\mu^{\mathrm{R}}_{\mathrm{ld}}$ is the residual potential of the larger particles, k is the Boltzmann constant, T is the absolute temperature, $\theta_{i\mathrm{d}}=\pi a_{i\mathrm{d}}^2 N_{i\mathrm{d}}/S$ is the disk surface coverage, i=l,s, $a_{i\mathrm{d}}$ and $N_{i\mathrm{d}}$ are the radius and number of the adsorbed disks, respectively, $\theta_{\mathrm{d}}=\theta_{\mathrm{ld}}+\theta_{\mathrm{sd}}$, and $\gamma=a_{\mathrm{ld}}/a_{\mathrm{sd}}$ is the disk size ratio. It should be noted that Eq. (7) describes a two-dimensional system only.

However, a useful approximation of the hard-sphere adsorption can be formulated by redefining the geometrical parameter γ. Expanding Eq. (7) in the power series of $\theta_{i\mathrm{d}}$ (up to the order of two), we obtain the expression

$$B_{\mathrm{ld}} \cong 1 - 4\theta_{\mathrm{ld}} - (\gamma+1)^2\theta_{\mathrm{sd}}, \tag{8}$$

valid for low surface coverage. In the case of the bimodal spheres system, it can be deduced from geometrical considerations that at low coverage the large-particle ASF is equal to

$$B_{\mathrm{l}} \cong 1 - 4\theta_{\mathrm{l}} - 4\lambda\theta_{\mathrm{s}}, \tag{9}$$

where λ is the large-to-small sphere size ratio, $\lambda=a_{\mathrm{l}}/a_{\mathrm{s}}$. Thus, Eqs. (8) and (9) can be matched when

$$\gamma = 2\sqrt{\lambda} - 1, \tag{10}$$

$\theta_{\mathrm{ld}}=\theta_{\mathrm{l}}$, and $\theta_{\mathrm{sd}}=\theta_{\mathrm{s}}$. Finally, we can conclude that the ASF for the large sphere in the bimodal spherical-particle system in the low-surface coverage limit can be approximated by the equation

$$\begin{aligned} B_{\mathrm{l}} = (1-\theta)\exp\Bigg[&-\frac{3\theta_{\mathrm{l}}+(4\lambda-1)\theta_{\mathrm{s}}}{1-\theta} \\ &-\left(\frac{\theta_{\mathrm{l}}+\left(2\sqrt{\lambda}-1\right)\theta_{\mathrm{s}}}{1-\theta}\right)^2\Bigg], \end{aligned} \tag{11}$$

where $\theta=\theta_{\mathrm{s}}+\theta_{\mathrm{l}}$.

Substituting $\theta_{\mathrm{l}}=0$ we can derive the analytical expression for the large-particle ASF corresponding to the initial adsorption flux of the large particles at surfaces precovered with the small ones:

$$B^0_{\mathrm{l}} = (1-\theta_{\mathrm{s}})\exp\left\{-\frac{(4\lambda-1)\theta_{\mathrm{s}}}{1-\theta_{\mathrm{s}}} - \left[\frac{\left(2\sqrt{\lambda}-1\right)\theta_{\mathrm{s}}}{1-\theta_{\mathrm{s}}}\right]^2\right\}. \tag{12}$$

Knowing B_{l}, we can calculate particle-adsorption kinetics from the constitutive dependence [2–7]

$$B_{\mathrm{l}} = \frac{\mathrm{d}\theta_{\mathrm{l}}}{\mathrm{d}\tau}. \tag{13}$$

This equation can be formally integrated to the form

$$\theta_{\mathrm{l}}(\tau) = \left[\int_0^{\theta_{\mathrm{l}}} \frac{\mathrm{d}\xi_{\mathrm{l}}}{B_{\mathrm{l}}(\xi_{\mathrm{l}})}\right]^{(-1)}, \tag{14}$$

where $[f(x)]^{(-1)}$ represents the inverse function of the function $f(x)$ and ξ_{l} is a dummy integration variable. It should be mentioned that Eq. (14) adequately describes the adsorption kinetics only in a system where both bulk

transport and the hydrodynamic scattering effect can be neglected.

2.3. Results of computation

Using the above RSA algorithm, we performed extensive calculations to determine the ASFs, adsorption kinetics, jamming coverages, and the structure of the large-particle adsorbed layer. We verified the effect of the particle size ratio and the small-particle surface coverage on the characteristics of the adsorption process, and we compared the obtained numerical results with the analytical approximations described above. The results that allow quantitative analysis of the adsorption process are presented below.

2.3.1. Available surface function

The quantity of considerable interest is the blocking function B_1^0, which characterizes the initial adsorption kinetics of large particles at precovered surfaces. In Fig. 1 the dependence of this function on the small-particle surface coverage is shown for $\lambda=1$ (reference curve for monodisperse system), 2.2, 5, and 10. As will be noticed, the influence of preadsorbed small particles on the initial flux (B_1^0 function) is significantly more pronounced for larger values of the λ parameter. This "surface-poisoning" effect is further illustrated by the data shown in Fig. 2. It is interesting to note that the numerical data are well reflected by analytical Eq. (12) at low to medium surface coverage $\theta_s<0.2$, and that the RSA-calculated ASF is smaller than the ASF of the large particle adsorbed at equilibrium. The theoretical predictions shown in Figs. 1 and 2 suggest that the presence of trace amounts of small particles often invisible under an optical microscope can exert a profound

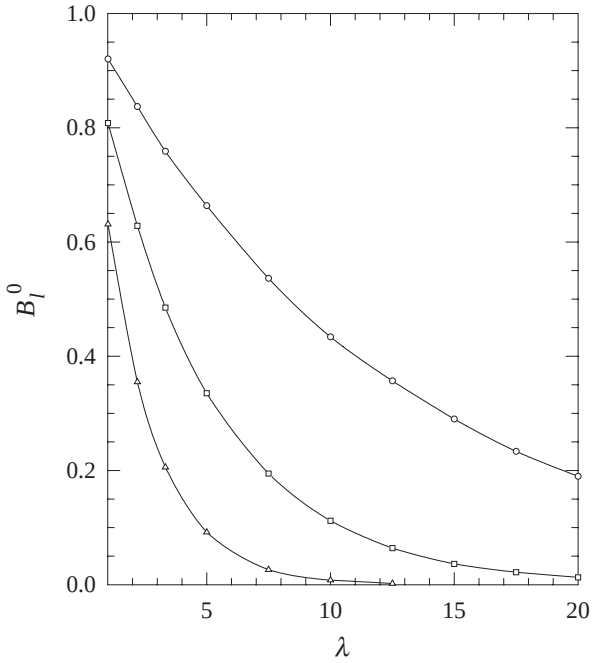

Fig. 2. Effect of the particle size ratio λ on the initial adsorption flux B_1^0 calculated for the small-particle surface coverage $\theta_s=0.02$ (circles), $\theta_s=0.05$ (squares), and $\theta_s=0.10$ (triangles) using Eq. (6).

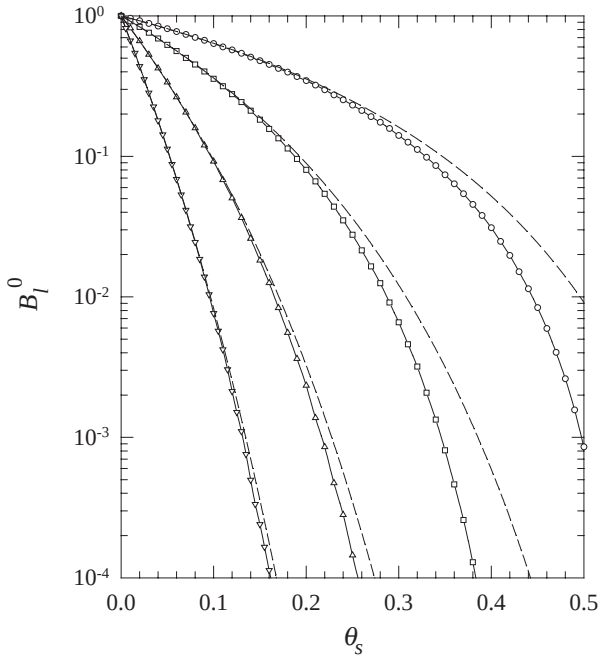

Fig. 1. Variation of the ASF B_1^0 (the initial adsorption flux) with the small-particle surface coverage. Dashed lines denote equilibrium results (Eq. (12)) and solid lines denote computer simulations (Eq. (6)) for the particle size ratio $\lambda=1$ (circles, reference curve), $\lambda=2.2$ (squares), $\lambda=5$ (triangles up), $\lambda=10$ (triangles down).

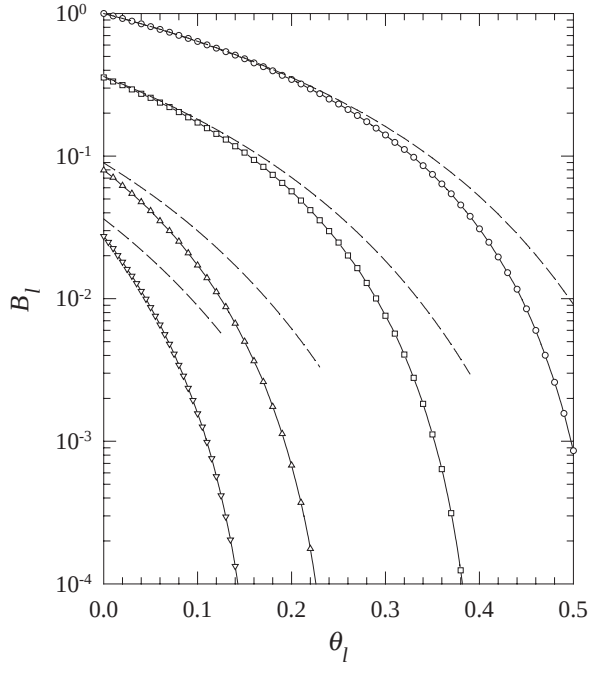

Fig. 3. Influence of the large-particle surface coverage θ_1 on the ASF B_1, as predicted by the SPT (Eq. (11), dashed lines) and numerical simulations (Eq. (6), solid lines). The curves correspond to the particle size ratio $\lambda=2.2$ and the small-particle surface coverage $\theta_s=0$ (circles, reference curve), $\theta_s=0.10$ (squares), $\theta_s=0.20$ (triangles up), and $\theta_s=0.25$ (triangles down).

effect on the adsorption kinetics (initial flux) of large particles, whose surface concentration can easily be measured directly (microscopically). We can therefore expect that by measuring the initial flux of large particles (of various sizes), we can detect the presence of small (invisible) particles.

The data shown in Figs. 1 and 2 are valid for the initial adsorption stage when the flux of the large particles remains steady. For longer times, however, accumulation of the large particles at the adsorption surface will lead to surface-blocking effects, which decrease the adsorption rate. The results plotted in Fig. 3 present the dependence of the B_1 function on the large-particle surface coverage for fixed θ_s values at $\lambda=2.2$. It can be seen that the presence of the small particles considerably reduces B_1. Unlike the equilibrium approximation of B_1^0, the large-particle ASF at the higher θ_1 is rather poorly approximated by the SPT, which significantly overestimates the numerical results, especially for $\theta_s>0.1$.

2.3.2. Maximum surface coverage

The kinetic curves, i.e., the θ_1 vs. τ dependencies derived from the numerical RSA simulations for $\lambda=5$, and various surface coverages of small particles are shown in Fig. 4. The analytical results based on the equilibrium SPT and calculated from Eq. (14) are also presented for comparison.

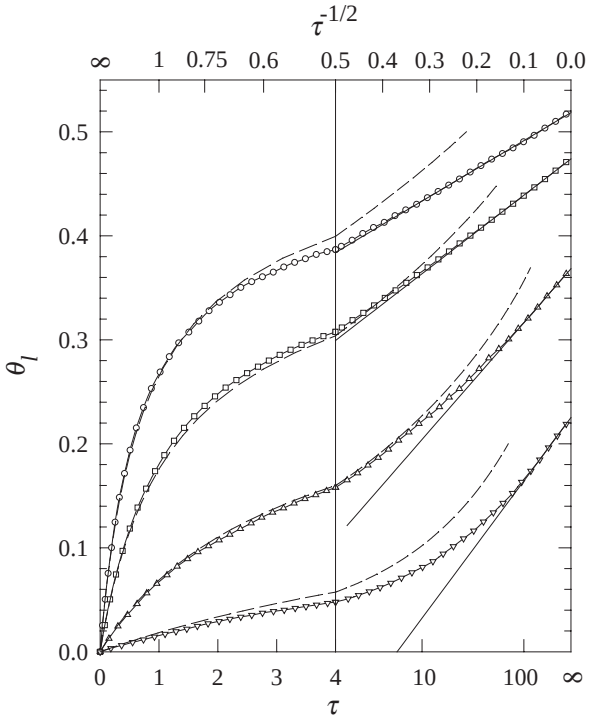

Fig. 4. Adsorption kinetics of the larger particle at the surface precovered with the smaller particles at the particle size ratio $\lambda=5$, expressed as θ_1 vs. τ dependencies: $\theta_s=0.02$ (circles), $\theta_s=0.05$ (squares), $\theta_s=0.10$ (triangles up), $\theta_s=0.15$ (triangles down). Open symbols denote the computer simulations. Dashed lines correspond to the SPT equilibrium results (Eqs. (11) and (14)). Solid lines depict the linear fits, i.e., $\theta_1^\infty-\theta_1\propto\tau^{-1/2}$.

As can be seen, the equilibrium model can be used as a reasonable estimate of adsorption kinetics on precovered surfaces for adsorption time $\tau<10$. For longer times, however, the equilibrium SPT results are overestimated. The adsorption kinetics at the initial stage is linear with the slope (initial flux) well reflected by Eq. (12). At $\tau>1$ the kinetic curves deviate significantly from linearity, indicating that the adsorption rate decreases. To present this long-time adsorption data more efficiently, we applied the θ_1 vs. $\tau^{-1/2}$ transformation, which compresses the infinite time domain into a finite one. This transformation has been used previously [4,5,20,43] for analyzing adsorption at homogeneous surfaces. As can be seen in Fig. 4, the numerical results plotted using this transformation can indeed be described by a straight-line dependence, although the range of this asymptotic regime decreases for higher values of θ_s. The linear dependence of θ_1 on $\tau^{-1/2}$ implies that the blocking parameter of the large particles B_1 is given by the expression

$$B_1\propto\left[\theta_1^\infty(\theta_s)-\theta_1\right]^3 \tag{15}$$

[28], where the large-particle jamming coverage θ_1^∞ is dependent only on the small-particle coverage θ_s. Thus, the jamming coverage has been calculated by fitting the numerical data (the θ_1 vs. $\tau^{-1/2}$ dependencies) by straight lines and subsequent extrapolation to $\tau^{-1/2}$ (adsorption time tending to infinity). Averages from five various computer runs have been taken in order to attain a sufficient precision of θ_1^∞.

Results collected in Fig. 5 present the dependence of θ_1^∞ on λ changed within the range of 1 to 20 at fixed values of θ_s equal to 0.02, 0.05, 0.10, and 0.20. We can observe in this figure that the presence of preadsorbed particles results in the monotonic decrease of the large-particle jamming coverage, although the effect becomes well pronounced only for $\lambda>4$ and $\theta_s>0.02$. For example, the change in the λ parameter from 5 to 20 at $\theta_s=0.05$ results in decrease of θ_1^∞ from 0.47 to 0.35. The net coverage $\theta_s+\theta_1^\infty$ drops in this case from 0.52 to 0.40. On the other hand, for $\theta_s=1.10$, the change in the λ parameter from 5 to 20 will exert a more significant effect on θ_1^∞, which will decrease from 0.37 to 0.02, whereas the net coverage decreases from 0.47 to 0.12.

Dependencies of the jamming concentrations θ_1^∞ on θ_s are also shown graphically in Fig. 6. For sake of convenience the total coverage, i.e., the sum $\theta_s+\theta_1^\infty$, is also plotted in the figure. The characteristic feature of the θ_1^∞ vs. θ_s dependencies is that they fall abruptly to very small values when θ_s is increased. The numerical results can be fitted by the interpolating functions (cf. dash-dot lines in Fig. 6)

$$\theta_1^\infty=\theta_\infty^{[c/(c-\theta_s)]^2}, \tag{16}$$

where $\theta_\infty=0.547$ is the jamming coverage for hard, monodisperse spheres, and c are the dimensionless constants equal to 0.596, 0.404, and 0.274 for λ equal to 2.2, 5, and 10, respectively.

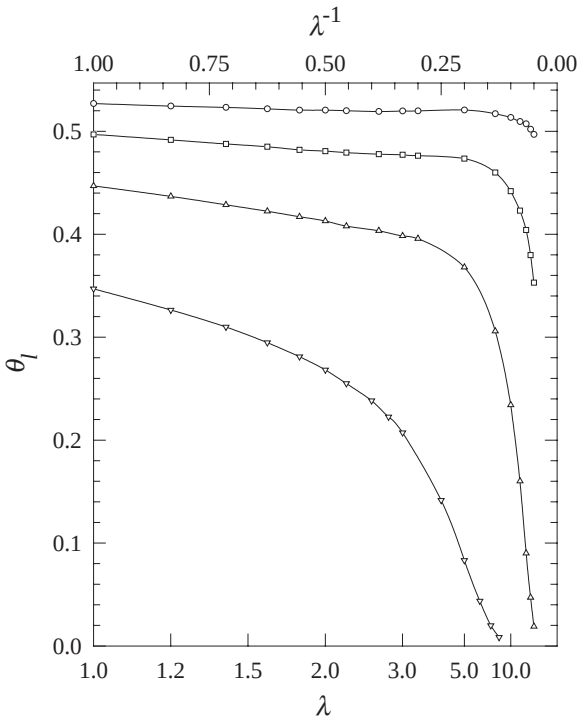

Fig. 5. The jamming limit θ_1^∞ as a function of the λ parameter at the small-particle surface coverage $\theta_s=0.02$ (circles), $\theta_s=0.05$ (squares), $\theta_s=0.10$ (triangles up), $\theta_s=0.20$ (triangles down). Numerical results were calculated by fitting the simulation data (θ_1 vs. $\tau^{-1/2}$ dependencies) by straight lines and subsequent extrapolation to $\tau^{-1/2}$.

On the other hand, in the large-particle low-coverage limit corresponding to the isolated targets regime, i.e., for $\theta_1^\infty<0.10$, one could expect that jamming coverage should be proportional to the initial ASF of the large particle and to its size. Indeed, the character of the numerical data can better be reflected by the interpolating function

$$\theta_1^\infty = c\lambda^2 B_1^0(\theta_s), \tag{17}$$

where $B_1^\infty(\theta_s)$ is the ASF function given by Eq. (12) and c represent the dimensionless constants equal to 1.718, 1.334, and 0.930 for λ equal to 2.2, 5, and 10, respectively. Another interesting feature of the data shown in Fig. 6 is that the net surface coverage of adsorbed particles passes through a minimum whose depth increases considerably for larger λ. We found the minimum coverages to be 0.378 for $\lambda=2.2$ ($\theta_s=0.34$), 0.261 for $\lambda=5$ ($\theta_s=0.24$), and 0.181 for $\lambda=10$ ($\theta_s=0.16$). These results represent a spectacular manifestation of the irreversibility effect since the composition and density of ''monolayers'' formed by particles is dependent on the peculiarities of the adsorption path, e.g., on the order that particles are brought to the interface. Physically, this effect can be realized by replacing the smaller particle suspension after a given adsorption time with the larger particle suspension.

The abrupt change in θ_1^∞ upon increase in λ or coverage of small particles θ_s (analogous to the change in the initial flux presented in Figs. 1 and 2) suggests that by measuring θ_1^∞ experimentally one can draw conclusions about the size and coverage of smaller sized particles. This ability means that surface homogeneity can easily be determined in a measurement of such type. It should be mentioned, however, that the jamming-coverage measurements are considerably more tedious than the kinetic measurements of the initial flux of larger particles.

2.3.3. Pair-correlation function

The presence of preadsorbed particles affects not only the kinetic aspects of larger particle adsorption but also the spatial distribution of larger-particle-forming monolayers. This phenomenon can be qualitatively observed in Fig. 7, where the "mixed" monolayers are shown obtained from numerical simulations for fixed large-particle coverage equal to 0.1 and various λ equal to 2.2, 5, and 10. It should be noted that for $\lambda>4$, adsorption of large particles might occur in such a way that the small particles are located underneath (shown in Fig. 7 by circles inside the large particles). This phenomenon reduces the surface-blocking effect in comparison with the adsorption of disks analyzed in Refs. [24,25].

Quantitatively, the effect of the small particles on the large-particle monolayer structure can be evaluated by determining the pair-correlation function of the large particles g_1 according to the method described above. As was demonstrated in [28,32], for all verified λ the shape of the pair-correlation function deviates considerably from the monodisperse counterpart. This effect is especially well

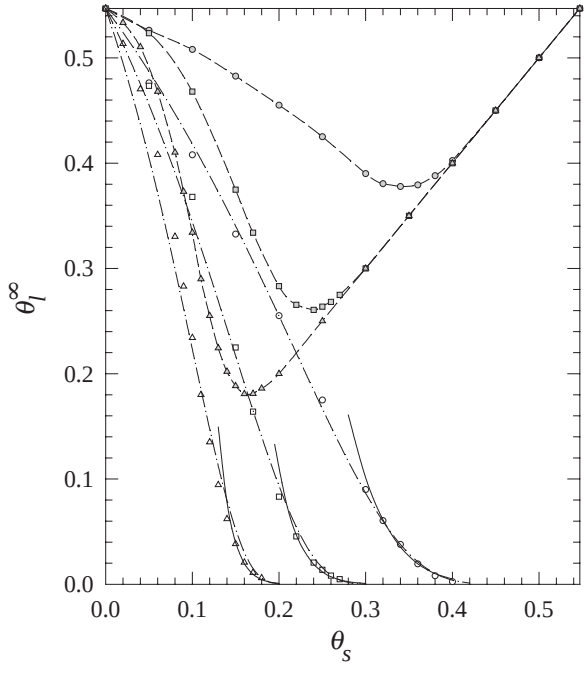

Fig. 6. The jamming limit θ_1^∞ as a function of the small particle surface coverage θ_s at $\lambda=2.2$ (circles), $\lambda=5$ (squares), and $\lambda=10$ (triangles). Open symbols are the numerical results determined from the linear fitting of the simulation data. Dash-dot lines represent the fitting functions given by Eq. (16). Solid lines show the limiting results calculated from Eq. (17). Dashed lines (or gray symbols) correspond to the net coverage $\theta_1^\infty+\theta_s$.

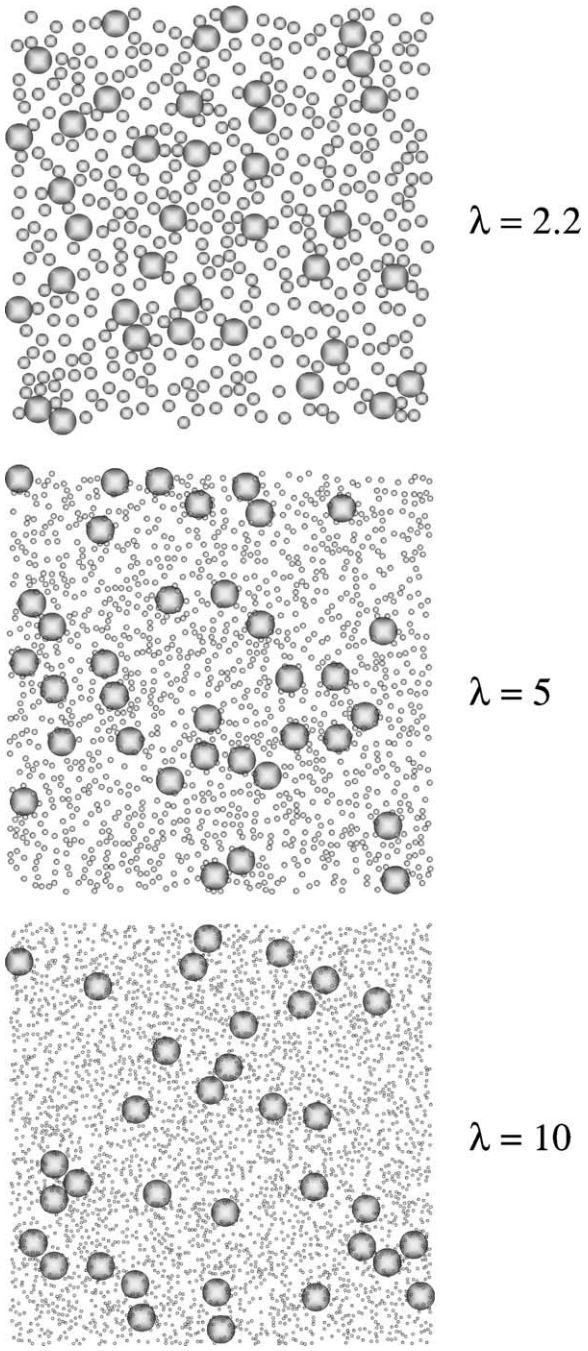

Fig. 7. Adsorbed particle "monolayers" close to jamming simulated numerically at the large-particle surface coverage θ_l=0.1 and various parameters λ and θ_s, i.e., λ=2.2 and θ_s=0.30, λ=5 and θ_s=0.20, λ=10 and θ_s=0.14. Note that the invisible, small background particles located below the larger particles are made visible to show their positions.

pronounced for λ=2.2 (see Fig. 8) when the g_l functions exhibit a maximum increasing with θ_s, located at the dimensionless distance r/a_1 equal about 2.8. The position of this maximum agrees quite well with the separation distance between two large particles with one small particle in between, which can be calculated from simple geometry as $4/\sqrt{\lambda}$. Thus, for λ=2.2, r/a_1 equals 2.7, which corresponds well to the above value determined from

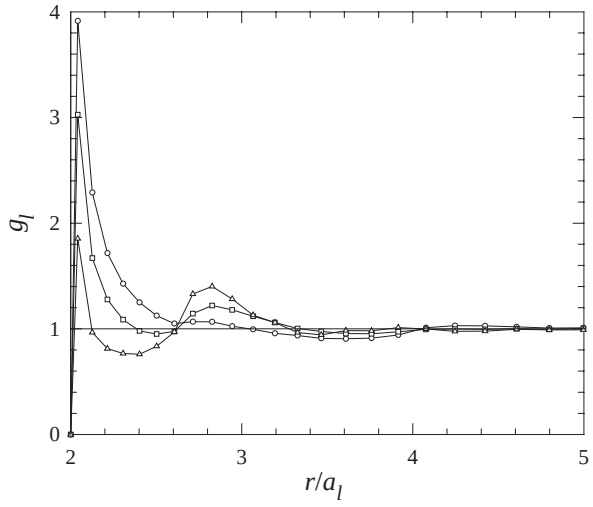

Fig. 8. Radial distribution functions $g_l(r/a_1)$ calculated using Eq. (3) for the particle size ratio λ=2.2 and the small-particle surface coverage θ_s=0.10 (circles), θ_s=0.20 (squares), and θ_s=0.30 (triangles) close to jamming. The large-particle surface coverage equals θ_l=0.41, θ_l=0.25, and θ_l=0.09, respectively.

simulations. From simple geometrical considerations we can also deduce that for λ>4 the small particles cannot prevent the larger ones from approaching each other closely. Thus, the secondary maximum of the g_l function should be absent, which is confirmed by the data presented in Fig. 9.

The results concerning the distribution of large particles over a random monolayer shown in Figs. 7–9 suggest, therefore, that the presence of smaller particles (causing surface heterogeneity) may be detected by determining the pair-correlation functions of large particles, used as markers. However, the differences in monolayer structure are most pronounced for large-particle coverage close to jamming, which makes such measurements rather tedious.

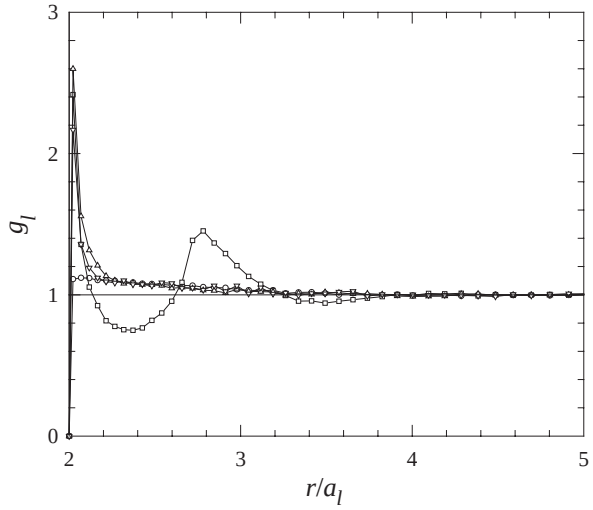

Fig. 9. Radial distribution functions $g_l(r/a_1)$ calculated using Eq. (3) for the large-particle surface coverage θ_l=0.1 (close to jamming) and the particle size ratio λ=1 (reference curve, circles), λ=2.2 (squares), λ=5 (triangles up), and λ=10 (triangles down). The corresponding small-particle surface coverage equals θ_s=0, θ_s=0.127, θ_s=0.191, and θ_s=0.291, respectively.

The above theoretical data are strictly valid for hard particles, i.e., for the case when the repulsive interaction range remains much smaller than particle size a_s. This situation can be realized experimentally at high ionic strength of the particle suspension, which is usually the case in protein adsorption studies mimicking physiological conditions. However, for lower ionic strength, the interaction range may become comparable with particle dimensions. In this case the particle–particle and particle–interface electrostatic interaction should be taken into consideration.

3. The electrostatic interaction models

An exact determination of the interaction energy between particles near the adsorption surface in general case seems prohibitive because of the inherent many-body problem. However, as demonstrated in Ref. [23], in the case of short-ranged interactions and not very low surface potentials, the van der Waals attraction can be negligible, and the superposition approximation of the electrostatic interaction can offer satisfactory accuracy of the total particle potential at the precovered collector surface. Usually, the inaccuracy of this approximation may be estimated as a ratio of the dispersion to electrostatic interaction. In stable colloidal systems that are of our interest, the inaccuracy is often smaller than 1% for an energetically important surface-to-surface distance. Even with this simplification, including electrostatic interaction into the RSA model of adsorption at precovered surfaces is not an easy task. It should be remembered that RSA simulations exploit a Monte Carlo technique, strictly suitable for systems at equilibrium. Extending the technique to model transport-related or irreversible phenomena should carefully be considered to avoid unrealistic or unreasonable results. If the application of the RSA model to hard-particle systems seems to be theoretically justified and has been experimentally verified for 15 years, the two older models (2D and 3D) of electrostatic interaction applicable for the RSA algorithm, often exploited for interpretation of experimental results, are greatly simplified. Therefore, to evaluate applicability of the models, we compare results derived from them with computations obtained based on the recently proposed, more sophisticated model CT [34]. In what follows we assume constant potentials on all surfaces.

3.1. 2D model

Historically, the first model of RSA allowing electrostatic interaction among colloid particles was proposed by Adamczyk et al. [20] and is known as the 2D RSA model. This model neglects the particle transport from the bulk, assumes the perfect sink (PS) particle–interface interaction, and adopts the Monte Carlo method of calculating the adsorption probability. It exploits the Boltzmann distribution for the interparticle potential and takes into account just the lateral electrostatic interaction force. The interaction energy is calculated according to the linear superposition approximation (LSA) [44] with a dimensionless coefficient α accounting for the interface effect on the particle–particle lateral interaction, expected to be of the order of 0.5. For two spherical particles of radii a_i and a_j, separated by the gap width h_m, the repulsive energy in the kT units is equal to

$$E_{ij}(h_m) = \alpha\varepsilon\frac{kT}{e^2}Y_iY_j\frac{a_ia_j}{a_i+a_j+h_m}\exp(-\kappa h_m), \quad i,j = 1,s, \tag{18}$$

where ε is the dielectric constant of the medium, e is the electron charge, $\kappa^{-1} = \sqrt{10^3\varepsilon kT/(8\pi e^2 I N_A)}$ is the Debye screening length in centimeters, I is the electrolyte ionic strength expressed in mol/dm^3, N_A is Avogadro's number, and Y_i and Y_j are the effective surface potentials of the particles given by equation [45]

$$Y_m = \frac{8tgh\left(\overline{\psi}_m/4\right)}{1+\sqrt{1-\frac{2\kappa a_m+1}{(\kappa a_m+1)^2}tgh^2\left(\overline{\psi}_m/4\right)}}, \quad m = i,j, \tag{19}$$

where $\overline{\psi}_m = \psi_m\frac{e}{kT}$ is the dimensionless surface potential of the particle m, and ψ_m is its surface potential.

Obviously, in the case of a very thin electric double layer, $\alpha = 1$, while for $\kappa a_i < 10$ it is reasonable to expect $\alpha < 0.5$. Thus, α can be considered as a fitting parameter allowing for some kind of correction for the surface interaction. It should be noted that calculation of its exact value is not usually crucial, because the interparticle potential used in the model is mostly determined by the exponential term appearing in Eq. (18).

As discussed in Ref. [34], the 2D RSA model seems to be a reasonable approximation in a system where the attractive (driving) force can be considered as much smaller than the repulsive particle–particle force, even close to the adsorption surface, and thus corresponding to the PS model. This condition is fulfilled to a reasonable extent in the case of a very low surface potential of the interface, although the problem of particle surface diffusion or adsorption reversibility can arise in such a system. If the condition is not obeyed, however, the repulsive interparticle interaction can be reduced because of the strong particle attraction to the interface. Such a situation arises especially when a large particle approaches the homogeneous interface next to a smaller, like-charged particle. Therefore, one may expect that the surface-blocking effects predicted for adsorption on precovered surfaces using the 2D RSA model can be overestimated.

3.2. 3D model

The second RSA approach allowing electrostatic interaction, called the 3D RSA model, was proposed by Oberholzer et al. [23] and then extended to bimodal systems by Weroński [33]. Unlike the 2D model, this approach

considers the particle transport from the bulk, assuming that neither electrostatic interaction nor Brownian motion causes a shift in the lateral position of the adsorbing particle as it moves toward the collector surface. During this motion, the total particle potential can be calculated according to the formula

$$E_i(h) = \sum_{m=1}^{n} E_{ij}(h_m) + E_{ip}(h), \quad i,j = 1,\mathrm{s}, \tag{20}$$

where h is the particle–interface gap width, n is the number of the small and large particles attached to the collector surface in the vicinity of the adsorbing particle, h_m is the minimum surface-to-surface distance between the moving particle and the deposited particle m, E_{ij} is the electrostatic (repulsive) interaction energy between them, and E_{ip} is the electrostatic (attractive) interaction energy between the particle and the collector surface. For the research described in this paper, all electrostatic particle–particle interactions in the system were calculated using Eq. (18) derived from the LSA with $\alpha = 1$. The attractive electrostatic energy between the traveling spherical particle and the adsorption surface is given by the limiting forms of Eqs. (18) and (19) when one of the particles' radii tends to infinity.

In general, a total interaction energy profile $E_i(h)$ is produced by a combination of the repulsion exerted by the attached particles with the attraction exerted by the surface. As a consequence, the profile has a maximum $E_b(x_v, y_v, x_1, y_1, \ldots, x_n, y_n)$, which represents a kinetic barrier to adsorption of the virtual particle. Its height depends on the configuration of deposited small and large particles. Using the Boltzmann distribution, we can calculate the particle adsorption probability at the given point of the adsorption surface. Fig. 10 presents the total interaction energy profiles corresponding to the simplest system, in which the large particle moves toward the surface next to the small, adsorbed particle. We assume the following parameters: $a_s = 250$ nm, $a_l = 625$ nm, $\psi_s = \psi_l = -50$ mV, $\psi_p = 100$ mV, and $I = 10^{-4}$ M. The profiles correspond to three different values of the particle center-to-center distance projection length $r_2 = \sqrt{(x_l - x_s)^2 + (y_l - y_s)^2}$. Based on the plots, we can conclude that the energy barrier occurs at some height above the adsorption surface and that the barrier height increases when the projection length r_2 decreases.

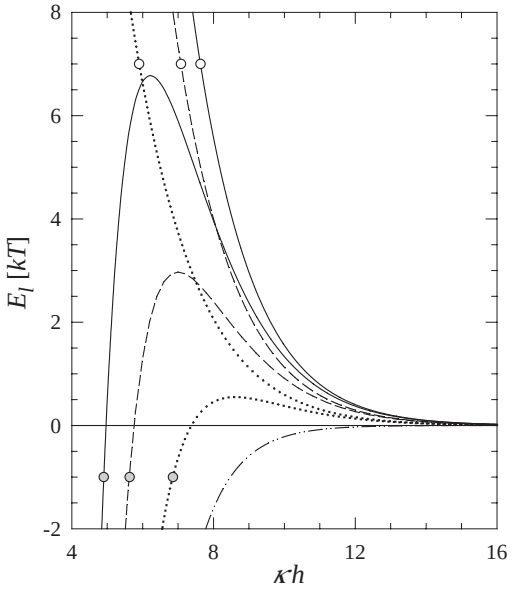

Fig. 10. Electrostatic interaction energy profiles calculated for the large particle approaching the surface next to the small particle in 3D RSA. The plots represent results based on Eq. (20). The dash-dot-dot line depicts the large-particle/interface attraction. The empty and gray circle indicates the particle–particle repulsion and the total energy profiles, respectively. Dotted, dashed, and solid lines correspond to $r_2 = r_0 + 2/\kappa$, $r_2 = r_0 + 1.2/\kappa$, and $r_2 = r_0 + 0.8/\kappa$, respectively, where $r_0 = 2\sqrt{a_s a_l}$. See more detail in the text.

Although the authors of Ref. [23] claim that the 3D RSA model is more realistic, we should remember that physics of this approach is still greatly simplified. The assumption that the particle trajectory is perpendicular to the interface seems artificial, especially for a particle overcoming the energy barrier, where the lateral component of the repulsive particle–particle force dominates. We can expect that according to the Boltzmann distribution most of the particles passing the energy barrier have low kinetic energy and therefore move in the direction of the lateral force. Thus, although the 3D RSA model seems to be a reasonable approach for studies of kinetic aspects of adsorption phenomena, it fails to provide appropriate monolayer structures. Consequently, we can suppose that computed jamming limits might be inaccurate as well.

3.3. CT model

Recently a new, extended RSA model that includes electrostatic interaction was proposed by Weroński [34]. The model, called CT RSA, has been based on the 3D RSA model. To avoid the discrepancy inherent in the assumption of the linear trajectory of the adsorbing particle, the virtual-particle trajectory is calculated according to the forces acting on the particle, starting from the point where the energy barrier was found (see Fig. 11). In the simplest formulation of this model, the trajectory is determined assuming the mutual compensation of hydrodynamic and dispersion forces between the interface and the particle approaching it. Further, particle–particle hydrodynamic and dispersion interactions, external forces, and rotational motion as well as convection and Brownian motion in the thin layer are neglected. Therefore, the virtual-particle trajectory can be calculated by integrating the deterministic equation of motion

$$\frac{\mathrm{d}\mathbf{r}_i}{\mathrm{d}t} = \frac{D_i^{\infty}}{kT}\mathbf{F}_i(\mathbf{r}_i) \tag{21}$$

over time, where $\mathbf{r}_i$ is the virtual-particle position vector, t is the time, $D_1^{\infty} = kT/6\pi\eta a_i$ is the diffusion coefficient of the particle in the bulk, η is the solution dynamic viscosity, and

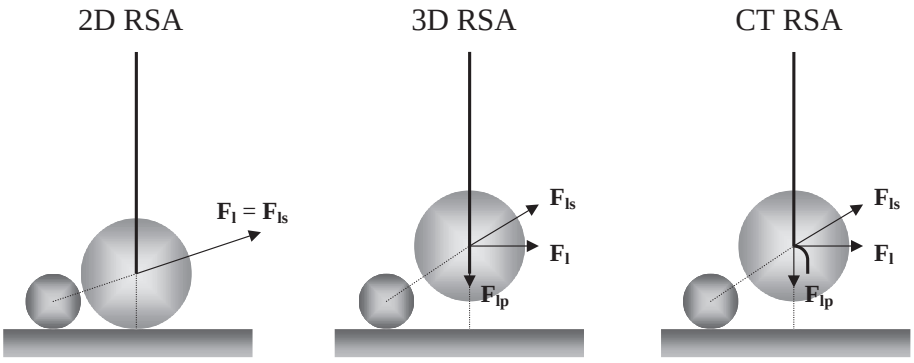

Fig. 11. Three different approaches of random sequential adsorption at precovered surfaces. Bold lines depict trajectories of the large-particle center considered in the models. The schemes show the large spherical particle at the energy barrier, where the adsorption probability is calculated. $\mathbf{F}_l$ represents the net force acting on the particle at the barrier. Note that because of the smaller particle–particle distance in the 2D RSA model, this approach predicts much stronger repulsion than the 3D and CT models. Unlike the 3D model, the CT RSA model assumes that immediately after crossing the energy barrier, the adsorbing particle begins to move curvilinearly.

$\mathbf{F}_i$ is the net force acting on the particle calculated according to the equation

$$\mathbf{F}_i(\mathbf{r}_i) = -\nabla E_i(\mathbf{r}_i), \tag{22}$$

where $E_i(\mathbf{r}_i)$ is the total particle potential given by Eq. (20).

It should be noted that the probability of particle adsorption at the final point can be considered as equal to the probability of its appearing at the starting point of the trajectory, calculated according to the Boltzmann distribution as in the 3D model. Actually, because of a complicated monolayer structure at high surface coverage, some of the virtual particles (one per a few thousand trials) are driven far from the adsorption surface. Therefore in practice a limiting distance must be introduced to the simulation algorithm, usually corresponding to a weak particle–interface interaction on the order of $10^{-2}\,kT$. If no energy barrier exists at the chosen virtual coordinates x_v, y_v, then no tracing is conducted and the virtual particle is adsorbed at this point, unless another adsorbed particle prevents it. In the latter case, the starting point of the virtual-particle trajectory and the probability that the particle will appear there are calculated at the height corresponding to the particles contact.

There is no conceptual difficulty in incorporating thermal motion, convection, or other types of interaction into the model, although incorporation may require some modification of the method used for choosing the particle's starting position. Eq. (21) then becomes the stochastic Langevin-type equation underlying the Brownian Dynamics (BD) method [46]. Therefore, using the more sophisticated equations leads to a "smart" BD model. In spite of rapid development in computer technology, however, the computational expense of such simulations is still high, which makes the simple CT RSA model attractive and useful.

4. The effective hard-particle approach

If the required accuracy of computation is not very high, the modeling of the electrostatic interaction can be simplified by exploiting the EHP concept. This method, originally developed for calculating the structure of real fluids [47–50] and offering considerable advantages over the direct method of soft-particle simulation, has often been exploited for modeling colloid phenomena [20,22,51–53], too. Instead of making complicated and time-consuming computations of particle energy, the EHP algorithms take into consideration a simple overlapping test in which the real, geometrical particle dimensions are replaced with the effective ones. Apart from simplifying algorithms and achieving a large computational gain, the EHP approach allows comparison with analytical solutions, which are often known for hard-particle systems, and thus yields a simple test for validating numerical results. It is worthwhile to note that the algorithms are independent of the method used for calculating the effective geometrical parameters. Below we discuss two methods of calculating the effective hard-particle diameter for monodisperse spherical particles and extending of the EHP approach to bimodal systems.

4.1. Monodisperse systems

The rigorous theoretical method of determining the relationship between the idealized hard-sphere model and the smoothly varying repulsive forces found in real fluids was developed based on the idea proposed by Zwanzig [47], which consists in treating the intermolecular forces in a fluid as perturbations on a hard-core potential. Since then, several authors have developed various perturbation theories, introducing improved models of the EHP. In our consideration we will use the Barker–Henderson model [50]. According to this model, the EHP diameter is equal to

$$d_{ii}^{*} = \int_0^{\infty} \{1 - \exp[-E_{ii}(r)]\}\mathrm{d}r, \quad i = \mathrm{s,l}, \tag{23}$$

where $r = 2a_i + h_1$, and h_1 is the minimum particle surface-to-surface distance.

In general, the energy E_{ii} can be a complicated function of the center-to-center distance r, and the integral appearing

in Eq. (23) must be computed numerically. It should be mentioned that Eq. (23) was derived assuming short-range interactions. This approximation has successfully been applied to a description of fluids and colloidal suspensions. The model was extended and effectively exploited for nonspherical particles as well [22].

Another more intuitive approach was proposed and used mostly by researchers conducting experimental studies of colloids [51–53]. Motivated by the fact that any force becomes important as soon as the work of that force is on the same order as thermal energy, some authors have chosen αkT (with $\alpha \approx 1$) as the value of the particle–particle potential at which to fix the effective hard-sphere diameter:

$$d_{ii}^* = r^*, \quad E_{ii}(r^*) = \alpha. \tag{24}$$

The value of α has often been obtained by fitting experimental results to a hard-particle model. This method was effectively used for spheroidal particles [53] as well.

As was demonstrated in Refs. [33,54], the results of the thermal energy approach are almost identical to those predicted by the Barker–Henderson model when $\alpha = 0.5$, which corresponds to the characteristic energy for one component of the three-dimensional translation Brownian motion.

4.2. Extension of the EHP approach to the bimodal systems

The EHP approach can easily be extended to a bimodal system. To do so, it is convenient to introduce the EHP center-to-center distance projection length d_{ij}^* as a generalization of the EHP diameter d_{ii}^*. Using the Barker–Henderson approximation and the 2D RSA model we may define the lengths by the equation

$$d_{ij}^* = \int_0^\infty \{1 - \exp[-E_{ij}(r_2)]\} \mathrm{d}r_2, \quad i,j = \mathrm{s,l}, \tag{25}$$

where $r_2 = \sqrt{(x_i - x_j)^2 + (y_i - y_j)^2} = \sqrt{r^2 - (a_i - a_j)^2}$ is the actual particle center-to-center distance projection length.

On the other hand, using the thermal energy approximation we have

$$d_{ij}^* = r_2^*, \quad E_{ij}(r_2^*) = 0.5. \tag{26}$$

In the case of the 3D RSA model, the Eqs. (25) and (26) involving the particle–particle energy E_{ij} should be replaced with the equations

$$d_{ij}^* = \int_0^\infty \{1 - \exp[-E_b(r_2)]\} \mathrm{d}r_2, \quad i,j = \mathrm{s,l}, \tag{27}$$

and

$$d_{ij}^* = r_2^*, \quad E_b(r_2^*) = 0.5, \tag{28}$$

respectively.

It should be noticed that because of a curvilinear particle trajectory in the CT RSA model, the starting and ending x, y particle coordinates are different in general. The values obtained from Eqs. (27) and (28) correspond to the starting points of the effective particle trajectories and thus should be suitable for estimating the ASF. On the other hand, considering the structural aspects of adsorption requires taking into account the effective final positions of the adsorbing particles. However, the main driving force acting on the particles approaching the interface is not diffusion but rather strong electrostatic attraction in the thin layer adjacent to the interface. Therefore, the equilibrium approach presented above does not seem to be reasonable for predicting the effective final particle position. Instead we can approximate the effective final distances with the values that correspond to the effective starting positions and can be found using Eq. (21). In what follows we will use d_{ij}^* to denote the final distance projection length corresponding to the effective starting distance.

In general, the EHP dimensions calculated using the above methods are nonadditive in the sense that the condition $d_{\mathrm{ls}}^{*2} = d_{\mathrm{ll}}^* d_{\mathrm{ss}}^*$, resulting from the simple geometry of two contacting spheres on a planar surface, is not obeyed. This situation makes further analysis more complicated. Therefore, to ensure additivity of the effective particle dimensions, we will choose effective radii in such a way to have the system of the small EHPs and the effective interacting large particles (see Fig. 12). From the symmetry condition we have

$$a_{\mathrm{s}}^* = \frac{1}{2} d_{\mathrm{ss}}^*, \tag{29}$$

and from the Pythagorean theorem $d_{\mathrm{ls}}^{*2} + (a_{\mathrm{l}}^* - a_{\mathrm{s}}^*)^2 = (a_{\mathrm{l}}^* + a_{\mathrm{s}}^*)^2$ we get

$$a_{\mathrm{l}}^* = \frac{d_{\mathrm{ls}}^{*2}}{4a_{\mathrm{s}}^*} = \frac{d_{\mathrm{ls}}^{*2}}{2d_{\mathrm{ss}}^*}, \tag{30}$$

where variables with a star denote quantities corresponding to the effective particles.

The effective size ratio is given as

$$\lambda^* = \frac{a_{\mathrm{l}}^*}{a_{\mathrm{s}}^*} = \left(\frac{d_{\mathrm{ls}}^*}{d_{\mathrm{ss}}^*}\right)^2, \tag{31}$$

(see Fig. 13). As can be seen, the increase of the interaction range results in a decrease of the effective size ratio, in agreement with intuition. Surface coverage of the effective small and large particles equals

$$\theta_{\mathrm{s}}^* = \theta_{\mathrm{s}} \left(\frac{a_{\mathrm{s}}^*}{a_{\mathrm{s}}}\right)^2 = \theta_{\mathrm{s}} \left(\frac{d_{\mathrm{ss}}^*}{2a_{\mathrm{s}}}\right)^2 \tag{32}$$

and

$$\theta_{\mathrm{l}}^* = \theta_{\mathrm{l}} \left(\frac{a_{\mathrm{l}}^*}{a_{\mathrm{l}}}\right)^2 = \theta_{\mathrm{l}} \left(\frac{d_{\mathrm{ls}}^{*2}}{2a_{\mathrm{l}} d_{\mathrm{ss}}^*}\right)^2. \tag{33}$$

In the high electrolyte-concentration limit, expressed usually in terms of the large κa parameter, the electrostatic interaction becomes weak and the parameters d_{ij}^* tend to the

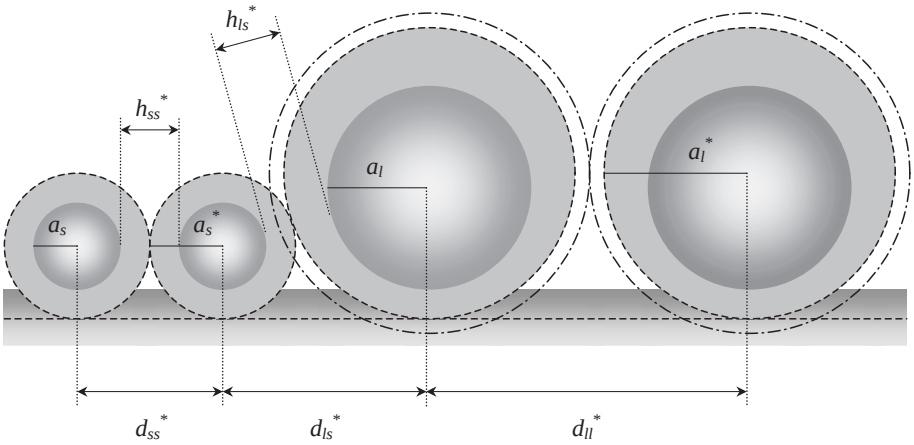

Fig. 12. Schematic description of the effective hard small- and soft large-particles at a plane interface. Dashed lines denote shapes of the effective particles and adsorption surface. Dash-dot lines show the effective interaction range of the large particles.

nonzero values $2\sqrt{a_i a_j}$. Therefore, in this range of the κa parameter, a logarithmic plot of the functions $d_{ij}^*(\kappa a)$ becomes unreadable. To avoid this inconvenience we will present the effect of the κa parameter on the effective particle size in terms of the effective minimum particle surface-to-surface distance

$$h_{ij}^* = \sqrt{d_{ij}^{*2} + \left(a_i - a_j\right)^2} - a_i - a_j, \tag{34}$$

expected to be roughly proportional to the electric double-layer thickness.

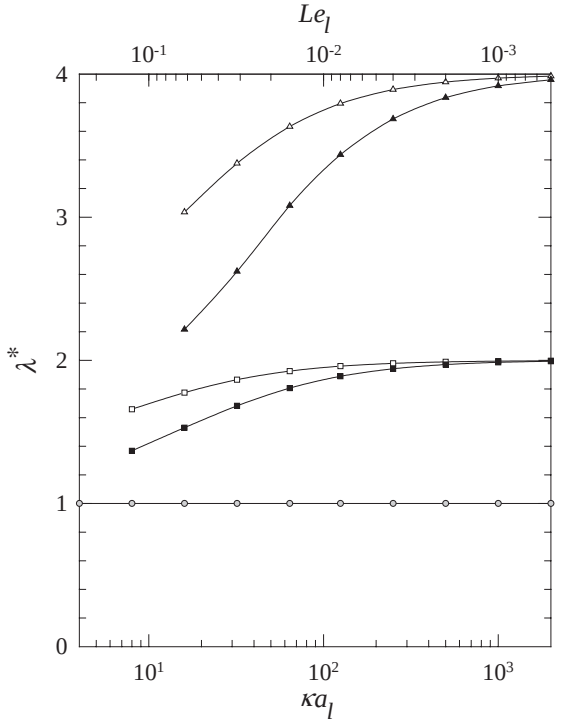

Fig. 13. Comparison of the effective particle size ratios as predicted by two models of RSA for $\lambda=1$ (reference curve, circles), $\lambda=2$ (squares), $\lambda=4$ (triangles). Open symbols refer to the model 2D (Eqs. (31) and (25)) and filled ones to the model 3D (Eqs. (31) and (27)). Gray symbols denote identical 2D and 3D results. $Le_l=1/\kappa a_l$.

5. Soft-particle systems

Here we focus on the effect of electrostatic interaction on colloid adsorption at surfaces precovered with smaller sized, like-charged particles. In our study we used most often the CT RSA model, which seems to be the most relevant. We also exploited the 2D and 3D RSA models to allow us to compare the results obtained using the three models. The definitions introduced in Section 2 for hard-particle systems are valid for the soft particles as well. However, interpretation of some of the variables becomes much more difficult. It is especially the case when we are dealing with the ASF that simple geometrical interpretation is no longer valid. We should also remember that terms such as “low” and “high” surface coverage refer rather to the effective hard particles instead of to the real, soft ones. Depending on the effective interaction range, this qualitative distinguishing becomes appropriate for more or less smaller surface coverage.

5.1. The simulation algorithm

Just as we did with the hard-particle algorithm, we carried out simulations over a square simulation plane with the usual periodic boundary conditions at its perimeter and two subsidiary grids of square areas (cells) of the size $\sqrt{2}a_s$ and $\sqrt{2}a_l$ [34]. This strategy enhanced the scanning efficiency of the adsorbing particle environment performed at each simulation step. The simulations were conducted in two main stages: first, adsorption of smaller particles at the homogeneous interface was carried out to a desired surface coverage θ_s; then, the larger particles were adsorbed at the prepared heterogeneous surface.

At both stages, the next particle to be adsorbed was selected by choosing at random its x_v and y_v center coordinates. Next, the vicinity of the virtual particle was scanned and the minimum distance h_0 to the interface, resulting from the nonoverlapping condition, was calcula-

ted. If the particle–interface potential at the minimum distance was larger than $E_{ip}(h_0) > -0.01$, the virtual particle was rejected and new particle coordinates were generated. Otherwise, the location and height of the kinetic barrier to adsorption E_b was calculated as described above, and the starting point of the particle trajectory was assumed to be at the barrier. If no energy barrier existed at the chosen virtual coordinates x_v, y_v, the component of the total force acting on the adsorbing particle at the distance h_0 perpendicular to the interface was verified. When the interaction was attractive, the particle was adsorbed at the point; otherwise, the starting point was assumed to be at the minimum distance h_0 and the total particle potential was calculated there. Based on the potential or barrier height, the probability of appearing of the particle at the starting point of the trajectory was calculated from the Boltzmann relationship. If the probability was smaller than an additional random number generated with uniform distribution within the interval (0;1), then the adsorption attempt was rejected and the next virtual coordinates were chosen. Otherwise, the particle trajectory was traced to the point of contact with the adsorption surface, where it was permanently fixed with no consecutive motion allowed. In rare cases the particle was driven far from the adsorption surface. If the particle–interface interaction dropped to 10^{-2} kT a new adsorption attempt was undertaken. Each particle path was calculated using the CT RSA model as described above, taking into account only neighboring particles and limiting the tested vicinity to a circle that includes all the adsorbed particles for which E_{ij} could potentially be larger than 0.01.

This algorithm enabled us to simulate adsorption kinetics in terms of the dimensionless adsorption time given by Eq. (5). As in the hard-particle simulations, the maximum dimensionless time attained in our simulations was 10^4, which required an overall number of trials on the order of 10^9–10^{10}. The extrapolation procedure used in the case of hard particles for estimating jamming limits was not valid in soft-particle simulations because of the nonlinearity of adsorption kinetics at very long adsorption times, as demonstrated in [33]. Therefore, we report the coverage achieved after $\tau = 10^4$ as the maximum surface coverage. ASFs were calculated using the above algorithm according to the method described by Schaaf and Talbot [5], as described in Section 2.

5.2. Analytical approximation

Just as in the case of hard-particle systems, we tested the results of the simulations in terms of the equilibrium adsorption approach. The extension of the EHP approximation to bimodal systems, described in Section 4, can be exploited to derive analytical formulae predicting the ASF for the effective, interacting large particle at the interface covered with the effective hard, small spheres. Starting from Eq. (9) and using elementary geometry, it is not difficult to find that

$$B_l \cong 1 - 4\left(\frac{d^*_{ll}}{2a^*_l}\right)^2 \theta^*_l - 4\lambda^* \theta^*_s. \tag{35}$$

Eqs. (35) and (8) can be matched when

$$\theta_{ld} = \left(\frac{d^*_{ll}}{2a^*_l}\right)^2 \theta^*_l, \quad \theta_{sd} = \theta^*_s,$$

and

$$\gamma = 2\sqrt{\lambda^*} - 1. \tag{36}$$

Substituting Eqs. (30)–(33) we get

$$\theta_{ld} = \left(\frac{d^*_{ll}}{2a_l}\right)^2 \theta_l, \quad \theta_{sd} = \left(\frac{d^*_{ss}}{2a_s}\right)^2 \theta_s,$$

and

$$\gamma = 2\frac{d^*_{ls}}{d^*_{ss}} - 1. \tag{37}$$

This result drives us to the conclusion that the large-sphere ASF in the bimodal interacting spherical-particle system in the low coverage limit can be approximated by the equation

$$B_l = (1-\theta_d)\exp\left[-\frac{3\theta_{ld} + \gamma(\gamma+2)\theta_{sd}}{1-\theta_d} - \left(\frac{\theta_{ld} + \gamma\theta_{sd}}{1-\theta_d}\right)^2\right], \tag{38}$$

where variables θ_{ld}, θ_{sd}, and γ are defined by Eq. (37).

The limiting analytical expression for the large-particle ASF corresponding to the initial adsorption flux of the large particles at surfaces precovered with the small ones, derived at $\theta_l = 0$, is

$$B^0_l = (1-\theta_{sd})\exp\left[-\frac{\gamma(\gamma+2)\theta_{sd}}{1-\theta_{sd}} - \left(\frac{\gamma\theta_{sd}}{1-\theta_{sd}}\right)^2\right]. \tag{39}$$

Eqs. (38) and (39) can further be exploited for calculating adsorption kinetics in the low surface coverage limit, as described above.

5.3. Results of computation

We used the CT RSA algorithm to perform extensive computer simulations of soft-particle adsorption at precovered surfaces. The ASFs, jamming limits, and pair-correlation functions were obtained for the following values of the system's physical parameters: the large- and small-particle density and surface potential $\rho_l = \rho_s = 0.05$ g/cm^3 and $\psi_l = \psi_s = 50$ mV, respectively; the adsorption surface potential $\psi_p = -100$ mV; the absolute temperature $T = 293$ K; the dielectric constant $\varepsilon = 78.54$; and the large particle radius $a_l = 500$ nm. We conducted computations for three values of the small-particle radius: $a_s = 125$, 250, and

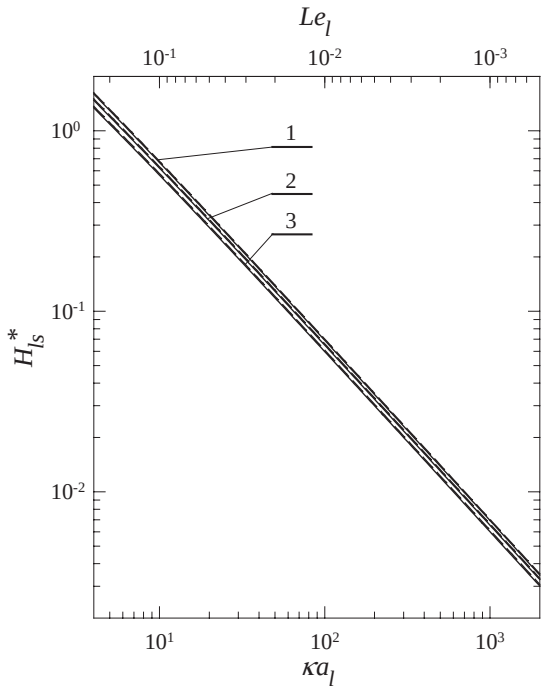

Fig. 14. Comparison of the effective minimum distances between small and large particle at a plane interface, calculated according to the 2D model in connection with two EHP approximations. Solid lines depict the Barker–Henderson approach (Eqs. (34) and (25)) and dashed ones represent the thermal energy approach (Eqs. (34) and (26)), respectively. The effective distances H^*_{ls} correspond to $\lambda=1$ (1), $\lambda=2$ (2), and $\lambda=4$ (3).

500 nm, corresponding to the parameter $\lambda=4$, 2, and 1. A few values of electrolyte concentration were chosen to demonstrate the effect of ionic strength. The values corresponded to the parameters $\kappa a_i=4$, 8, 16, 32, 64, 125, 250, 500, 1000, and 2000. The effect of the small-particle surface coverage was verified for $\theta_s=0$ (reference curves for monodisperse particle system), 0.02, 0.04, and 0.08. We compared the computations with the results stemming from the SPT extended to interacting spheres in 3D. We also exploited the two older models, 2D and 3D RSA, in the computations to allow comparison with CT RSA predicted results. It should be noted that at these particle sizes and density, the gravitational force acting on the particle is below 0.03 kT/a_i and therefore was neglected in our computations.

5.3.1. Effective minimum particle surface-to-surface distance

We studied the effect of ionic strength on the effective minimum particle surface-to-surface distance by using the three models of adsorption and the two approximations of the EHP. Fig. 14 presents the dependence of the normalized effective minimum distance $H^*_{ls}=h^*_{ls}/a_l$ on the κa_l parameter for three values of λ, as predicted by the 2D RSA model in connection with the two EHP approximations. The results based on Eq. (25) (the Barker–Henderson approach) and Eq. (26) (the thermal energy approach) clearly demonstrate that both approaches give almost identical results. As can be seen, the effect of λ is minor even at small values of κa_l, which suggests that the interface has little effect on particle adsorption, in line with the model's assumptions. The weak effect of the particle–interface interaction can also be deduced from the fact that the effective particle distances correspond well to the thermal energy 0.5 kT along the whole range of the parameter κa_l. This value confirms the assumption of particle lateral equilibrium at the interface and results from neglecting the fast, curvilinear particle transport in the thin surface-force layer adjacent to the adsorption surface. In the presented range of the κa_l parameter, the dependence $H^*_{ls}(\kappa a_l)$ is almost linear. The results are limited to the range corresponding to $\kappa a_s \geq 4$ to avoid inaccuracies resulting from many-body interactions.

The linearity is more obvious in Fig. 15 where the normalized effective minimum distance $H^*_{ss}=h^*_{ss}/a_s$ as a function of the κa_s parameter is depicted, as obtained from the linearized thermal energy approach, neglecting the preexponential term in Eq. (18). According to this approach, the effective minimum distance, corresponding to 0.5 kT particle–particle energy, is given by the equation

$$H^*_{ss} = \frac{1}{\kappa a_s} \ln\left(\frac{1}{2}\varepsilon\frac{kT}{e^2}Y_s^2 a_s\right). \quad (40)$$

As can be seen, the effective minimum distance can be calculated analytically and is proportional to the parameter

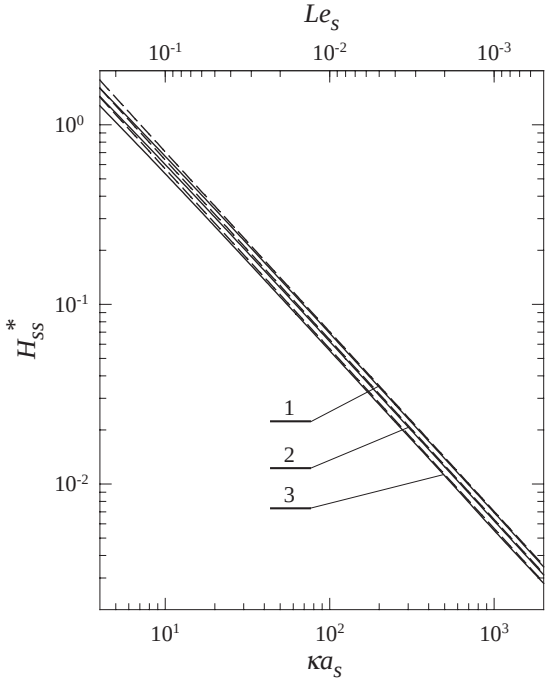

Fig. 15. Comparison of the effective minimum distances between two small particles at a plane interface, calculated according to the 2D model in connection with two EHP approximations. Solid lines depict the Barker–Henderson approach (Eqs. (34) and (25)) and dashed ones represent the linearized thermal energy approach (Eqs. (40)), respectively. The effective distances H^*_{ss} correspond to $a_s=500$ nm (1), $a_s=250$ nm (2), and $a_s=125$ nm (3). $Le_s=1/\kappa a_s$.

$Le_s = 1/\kappa a_s$. Comparison of the linearized approach and the nonlinear Barker–Henderson approximation shows that deviations of the function $H^*_{ss}(\kappa a_s)$ from linearity, as predicted from the 2D RSA model, are small and can be observed just at the small κa_s. The plots presented in Fig. 15 also demonstrate that the linearized thermal energy approach offers a good approximation of the effective minimum particle surface-to-surface distance.

As discussed above, the PS approximation exploited in the 2D RSA model seems to be valid just in the case of the large κa_i. Modeling adsorption in a system characterized by a larger interaction range, especially in a bimodal system, requires another approach. That is demonstrated in the next two figures, where the effect of ionic strength on the effective minimum interparticle distance is presented in the monodisperse and bimodal systems, using the 2D, 3D, and CT RSA models.

As can be seen in Fig. 16, in the case of monodisperse systems at high ionic strength ($\kappa a_s > 30$), both 2D and 3D models predict almost identical effective minimum distances, corresponding to the lateral interaction of about 0.5 kT. As discussed above, the value results from neglecting the nonlinear particle transport at the boundary layer. It should be kept in mind, however, that assuming the linear particle trajectories in the 3D model could result in artificial lowering of the effective interaction range. In fact, one can

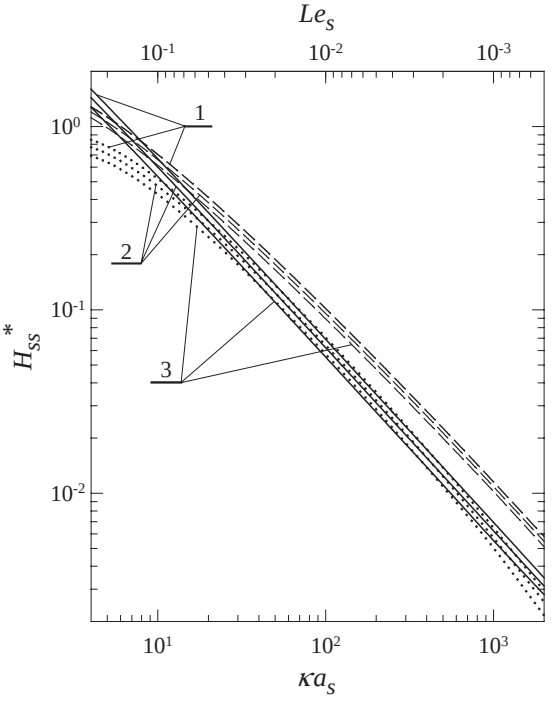

Fig. 16. Comparison of the effective minimum distances between two small particles at a plane interface, calculated according to the Barker–Henderson approximation in connection with three RSA models. Solid lines depict the 2D model (Eqs. (34) and (25)), dotted lines denote the 3D model (Eqs. (34) and (27)), and dashed ones represent the CT model (Eqs. (34) and (21)), respectively. The effective distances H^*_{ss} correspond to $a_s = 500$ nm (1), $a_s = 250$ nm (2), and $a_s = 125$ nm (3).

deduce that the net force acting on the particle at the energy barrier E_b is of the order $\kappa a_s E_b$ in the kT/a_s units and rapidly increases when the particle approaches the interface [34]. Taking into account that the barrier height corresponding to the effective particle distance is about $E_b \approx 0.5$, one can deduce that at $\kappa a_s > 10$, the driving force is much larger than the kT/a_s unit, which is characteristic for thermal motion [19]. Therefore, Brownian motion can be neglected in considering fast particle transport through the thin boundary layer at $\kappa a_s > 10$. Consequently, the equilibrium value of the interaction energy at the effective distance, as predicted by the 2D and 3D models, seems to have no solid support in theory.

On the other hand, in this range of κa_s the CT model predicts larger effective distances corresponding to the weaker particle–particle interaction. This prediction results from the fact that at the very beginning of the particle trajectory the lateral, repulsive component of the net force dominates and moves the particle out of its quasi-equilibrium starting position. Simultaneously the attractive component, perpendicular to the interface, increases rapidly and moves the particle toward the surface. At condition $\kappa a_s > 10$, however, the boundary-layer thickness is much smaller than the particle radius, and therefore the adsorbing particle cannot approach the adsorbed one closely during the small displacement. As a result, the final particle positions correspond to the interactions weaker than the thermal energy and to effective particle distances larger than predicted by the 2D and 3D models. It should be noted that at $\kappa a_s > 100$, the differences between the CT and 2D or 3D results become small in comparison to the particle size and can be hard to detect experimentally. Thus one can claim that in the short interaction range, all the models offer a reasonable accuracy.

At $\kappa a_s < 10$ the net driving force at the energy barrier corresponding to the effective particle surface-to-surface distance becomes comparable to the kT/a_s, unit and Brownian motion may have some effect on particle adsorption. It should be noted, however, that just in this range of κa_s the effective distances correspond to the thermal energy, which suggests that the CT model offers a quite reasonable approximation even at the interaction range comparable to the particle size, in spite of neglecting Brownian motion. At this range of interactions the effective particle distances predicted with the CT model become smaller than those predicted by the 2D model and correspond to the lateral repulsion few times stronger than the thermal energy. This final position of the adsorbing particle results from the thicker surface-force boundary layer. At the thicker layer, the particle located at the effective energy barrier there is at a relatively large distance from the interface. Also, the particle center-to-center distance projection length r_2 is relatively small in such a position. After a short distance, when the adsorbing particle is repulsed from its starting position and moves approximately parallel to the interface, the dominating attractive force directs the particle almost perpendicularly to the interface. As a result, the adsorbing

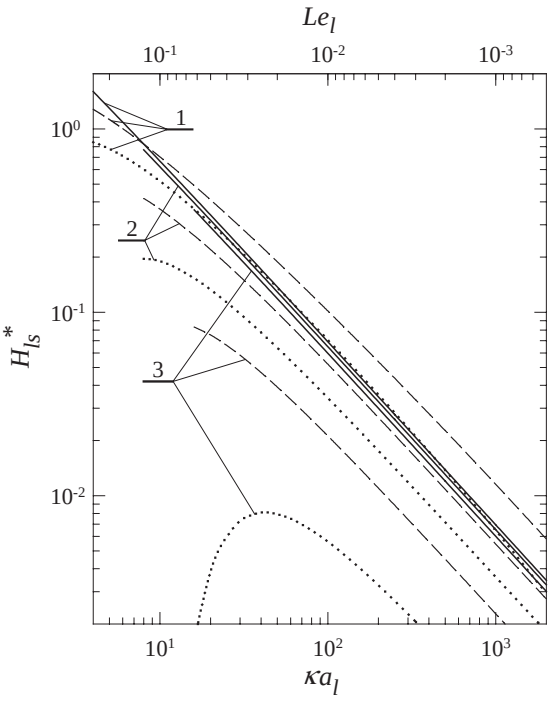

Fig. 17. Comparison of the effective minimum distances between small and large particle at a plane interface, calculated according to the Barker–Henderson approximation in connection with three RSA models. Solid lines depict the 2D model (Eqs. (34) and (25)), dotted lines denote the 3D model (Eqs. (34) and (27)), and dashed ones represent the CT model (Eqs. (34) and (21)), respectively. The effective distances H^*_{ls} correspond to $\lambda=1$ (1), $\lambda=2$ (2), and $\lambda=4$ (3).

particle approaches the deposited particle closely and the final position can correspond to a relatively high particle–particle potential.

As discussed above, the effective distance calculated with the 2D model corresponds to the lateral interaction on the order of thermal energy even at the smallest κa_s parameter, when the boundary-layer thickness becomes comparable to the particle dimension and one could expect the interface to have a strong effect. That value of the effective distance suggests overestimation of the results arising from the assumption of the constant parameter $\alpha=0.5$. The results obtained with the 3D model, on the other hand, corresponding to a lateral repulsion a few times stronger than kT, are evidently underestimated because of the assumption of linear particle trajectory.

The effect of the κa_1 parameter on the effective minimum particle surface-to-surface distance H^*_{ls} in the bimodal systems is presented in Fig. 17. As discussed above, the 2D RSA model predicts the interface to have little effect on particle adsorption even at low ionic strength. On the other hand, the effect is evident in case of the 3D and CT models in the whole range of κa_1. In agreement with intuition, the large particle can be deposited next to the small one even at a lateral repulsion on the order of 10 kT, as predicted by the CT model. This behavior results from the strong attraction of the large particle to the interface, which partially compensates the repulsion exerted by the small particle. On the other hand, the effective distances calculated with the 3D model correspond to the lateral interaction one to several orders of magnitude stronger than the thermal energy. Therefore, the linear trajectory assumption in the 3D model does not seem reasonable, driving us to the conclusion that the CT RSA model offers the best description of colloid-particle adsorption. It should be noted that h^*_{ij} obtained from the CT RSA model refers to the final position of the adsorbing particle and thus conveys information about the monolayer structure. On the other hand, h^*_{ij} calculated from the 3D RSA model corresponds to the ASF, almost identical for both 3D and CT processes, and so allows kinetic characterization of the systems. This capability is discussed in more detail below.

5.3.2. Available surface function

Comparison of the ASFs derived from the 2D, 3D, and CT RSA models and computed for the parameters $\lambda=2$ and $\kappa a_1=8$ is presented in Fig. 18. The functions, calculated according to Eq. (6), refer to the parameter $\theta_s=0$ (reference curve) and $\theta_s=0.08$. In agreement with intuition, both 3D and CT models give identical results at $\theta_s=0$ and low surface coverage of the large particle, which results from the similar construction of the algorithms. A small difference suggesting different monolayer structures becomes visible at $\theta_l=0.15$. The difference grows with increase of the surface coverage, so one could expect

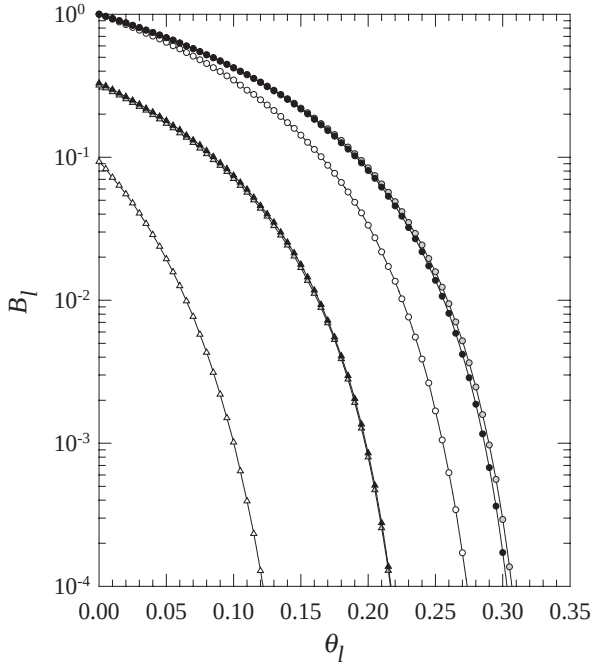

Fig. 18. Comparison of the ASFs $B_l(\theta_l)$ computed with three RSA models for the particle size ratio $\lambda=2$, parameter $\kappa a_1=8$, and two values of the small-particle surface coverage: $\theta_s=0$ (circles, reference curve) and $\theta_s=0.8$ (triangles). Open, gray and black symbols correspond to the results predicted with the 2D, 3D, and CT models, respectively, calculated with Eq. (6).

somewhat different jamming limits. As can be seen, the ASFs are always larger than their 2D counterparts, although the differences are very small at low surface coverage. This difference results from the fact that, unlike the 2D model, the 3D and CT models estimate the adsorption probability by taking into account the value of the particle potential calculated at some distance from the interface, and therefore at larger particle–particle distance. Moreover, the interparticle repulsion is partially neutralized because of the attraction to the interface. The 2D model neglects the three-dimensional effects. Therefore, it seems that application of the 2D model is limited to the monodisperse systems and low to medium surface coverage or high ionic strength ($\kappa a_s > 100$). On the contrary, the 3D model seems suitable for computing the kinetic aspects of adsorption in the full range of the κa_i parameters.

A similar behavior of the ASFs may be observed at $\theta_s = 0.08$. Because of the different structures of the small particles, however, a small difference between the 3D and CT models is visible at the low surface coverage θ_1 as well. Also, the difference between the predicted ASFs for the 2D and 3D models is much larger in the bimodal system and reaches three orders of magnitude. This discrepancy suggests that unlike the 3D model, the 2D one is useless in the case of bimodal systems. This conclusion is consistent with the experimental results published in Ref. [27]. Although the authors of this paper suggested that the reduced blocking effect observed during deposition on the precovered surface could result from the small-colloid-particle charge migration at the mica surface, in view of the results presented here we can explain the observed effect as being based on the reduction of the repulsion between different sized particles at the charged adsorption surface.

The result, which can be considered as an aspect of the reverse salt effect [55], consisted in the enhancement of the particle deposition rate under attractive double-layer forces and experimentally proved at the end of 1980s, is more evident in Fig. 19. The figure presents the initial deposition flux B_1^0 as a function of the κa_1 parameter calculated according to the CT model for $\theta_s = 0.02$ and 0.08, at $\lambda = 1$, 2, and 4. At the hard-particle limit ($\kappa a_1 = 2000$), the results are in agreement with approximate Eq. (9), apart from the two lowest curves corresponding to $\lambda = 2$ and 4 at $\theta_s = 0.08$, when $4\lambda\theta_s > 0.5$ and the assumption of low surface coverage does not apply anymore. In the long-interaction-range limit, on the other hand, the ASF's behavior depends on the λ parameter and is consistent with the dependences $H_{ls}^*(\kappa a_1)$, discussed above. At $\lambda = 1$, when H_{ls}^* is on the order of one, the ASFs monotonically and relatively quickly decrease with κa_1, which means that the particle–interface attraction has a minor effect on surface blocking. At $\lambda = 2$, when H_{ls}^* reaches few tenths, the large particle can be adsorbed at a much shorter distance to the small sphere, and so the blocking effect is reduced because of the stronger particle–surface attraction. Indeed, the corresponding ASFs' slopes are smaller than those when $\lambda = 1$, which confirms the statement. Finally, at

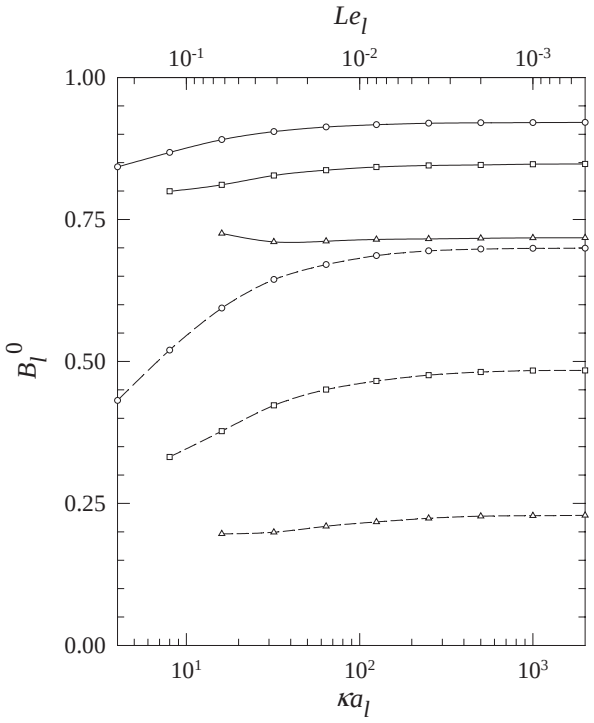

Fig. 19. Variation of the initial adsorption flux B_1^0 with the parameter κa_1 predicted by the model CT (Eq. (6)). Solid and dashed lines correspond to the small particle surface coverage $\theta_s = 0.02$ and $\theta_s = 0.08$, respectively. The particle size ratio equals $\lambda = 1$ (circles), $\lambda = 2$ (squares), and $\lambda = 4$ (triangles).

$\lambda = 4$ one can observe that B_1^0 changes very little with κa_1, which means that the interparticle repulsion is neutralized by the attraction to the interface. As a matter of fact, the corresponding H_{ls}^* is below 0.09, which confirms the weak blocking effect. Moreover, the value of B_1^0 computed at $\lambda = 4$, $\theta_s = 0.02$, and $\kappa a_1 = 16$, is larger than the corresponding hard-particle limit. This fact means that because of attraction to the interface, the particle can be adsorbed even if at the starting position it is located partially above the small particle at $r_2 < 2\sqrt{a_1 a_s}$, which would be impossible in a hard-particle system. It should also be noted that the effect of attraction to the interface is smaller at the higher coverage θ_s, which results from the enhanced repulsion exerted by the larger number of the smaller particles.

The effect of the small-particle surface coverage and particle size ratio on the B_1^0 ASF is investigated in Fig. 20. Both CT-model and equilibrium results (Eq. (39)) are presented there for $\kappa a_1 = 16$ and $\lambda = 1$ (reference system), 2, and 4. The results computed using the two models are essentially identical in the low-surface coverage limit, which confirms robustness of the software used for simulations. At higher coverage, however, the equilibrium ASFs achieve larger values, and the differences increase with the coverage θ_s. As in the hard-particle systems, the ASFs rapidly decrease with an increase in the λ parameter. A comparison of Fig. 20 with Fig. 1 makes it evident that the ASF's slope changes more in the soft-particle systems. At the low coverage θ_s, both hard- and soft-system ASFs have similar

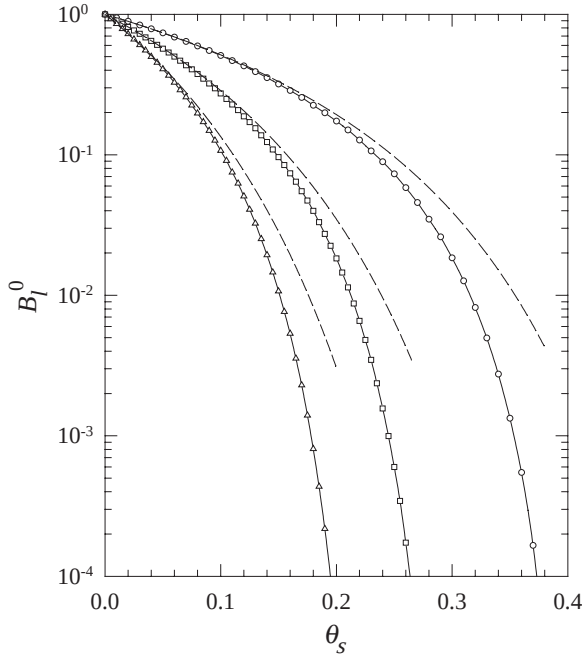

Fig. 20. Variation of the initial adsorption flux B_1^0 with the small particle surface coverage θ_s for the particle size ratio $\lambda=1$ (circles), $\lambda=2$ (squares), and $\lambda=4$ (triangles). Solid and dashed lines denote results obtained in numerical simulations (Eq. (6)) and using the SPT equilibrium approach (Eq. (39)), respectively.

slopes, which results from the mutual compensation of the repulsive and attractive electrostatic interaction. At the higher coverage, however, the interaction is dominated by the repulsion exerted by a larger number of the small particles, as discussed above, which results in the larger ASFs' slopes. In this range of coverage the electrostatic interaction can significantly increase the surface-poisoning effect, making it easier to detect the presence of smaller (invisible) particles by measuring the initial adsorption flux of larger particles, as discussed in Section 2.

However, a quantitative determination of the surface coverage of these particles becomes possible only by considering the coupling between the surface-layer transport (described by the function B_1^0) and the bulk transport (governed by convective diffusion of particles). According to the surface-force boundary-layer approximation [40], the actual initial particle flux j_1^0 in this case is governed by the generalized blocking function

$$\bar{B}_1^0(\theta_s) = j_1^0/j_1^{0,0} = \frac{KB_1^0(\theta_s)}{1+(K-1)B_1^0(\theta_s)}, \tag{41}$$

where $j_1^{0,0}$ is the initial adsorption flux to the homogeneous surface (at $\theta_s=0$) and $K=k_a/k_b$, k_a is the kinetic adsorption constant given by the equation

$$k_a = \left\{ \int_{\delta_m}^{\delta} \frac{\exp\left[\phi_{lp}(h')\right]}{D_l(h')}\,dh' \right\}^{-1}, \tag{42}$$

where δ is the thickness of the adsorbed small particle layer, ϕ_{lp} is the particle–interface potential, D_l is the position-dependent diffusion coefficient of the large particle, $h'=h+\delta_m$, and k_b is the bulk mass transfer rate. This rate can be calculated analytically or numerically for the stationary transport to uniformly accessible surfaces such as a rotating disk, impinging jet cells, etc. [36,56].

Expressing the diffusion coefficient as $D_l(h')=D_l^\infty h'/(h'+a_l)$ [14] and assuming the CT model of the electrostatic interaction, we can substitute $\phi_{lp}=E_{lp}$ and $\delta\approx 2a_s+h_{ls}^{0*}$, where h_{ls}^{0*} is the effective minimum particle surface-to-surface distance calculated for the isolated system of the small and large particles, located far from the interface. Then k_a can be evaluated explicitly to give

$$K = \left[Sh\left(\ln\frac{2/\lambda + H_{ls}^{0*}}{H_{lp}^{*}} + \frac{2}{\lambda} + H_{ls}^{0*} - H_{lp}^{*} \right) \right]^{-1}, \tag{43}$$

where $Sh=k_b a_l/D_l^\infty$ is the dimensionless mass transfer Sherwood number, $H_{ls}^{0*}=h_{ls}^{0*}/a_l$, and $H_{lp}^{*}=h_{lp}^{*}/a_l$ is the particle–interface gap width corresponding to $E_{lp}(h_{lp}^{*})=-0.5$. On the other hand, the PS approximation exploited in the 2D model gives

$$K = \left[Sh\left(\ln\frac{\delta}{\delta_m} + \frac{2}{\lambda} \right) \right]^{-1}. \tag{44}$$

As can be deduced from Eq. (41), the large particle flux (normalized to the flux for an uncovered surface) depends on two unknown parameters only,

$$j_1^0/j_1^{0,0} = f(\lambda,\theta_s), \tag{45}$$

which suggests that by experimental measurements of $j_1^0/j_1^{0,0}$ for various large particle sizes, we can determine both coverage θ_s and radius a_s of the small particle using a nonlinear fitting procedure.

Experimental data presented in Fig. 21, obtained for latex particles [3], confirm the validity of the above model, as well as the CT approach, for predicting the adsorption flux of larger particles at precovered surfaces. The experiments were conducted using the circular impinging jet cell and particles of 0.68 and 1.48 μm in diameter at $I=10^{-4}$ M and the Reynolds number $Re=4$. The dimensionless parameters were equal $\lambda=2.2$ and $\kappa a_l=24.55$. The surface potentials $\psi_s=\psi_l=-50$ mV and $\psi_p=50$ mV were assumed in the computer simulation, according to the experimental conditions, which gave the effective distances $H_{ls}^{0*}=0.305$ and $H_{lp}^{*}=0.360$. The Sherwood number obtained by the numerical solution of the convective diffusion equation was $Sh=0.0822$. Based on Eq. (43) we can calculate $K=5.88$.

The theoretical curve plotted in Fig. 21 is a good approximation of the experimental results in the whole range of the coverage θ_s. The only large discrepancy (one order of magnitude) between the observed and calculated value of the initial flux appears at $\theta_s=0.27$, which can be explained by considering small-particle size polydispersity. As estimated later on, the maximum coverage of the small particle is about 0.34 and so the θ_s should be considered

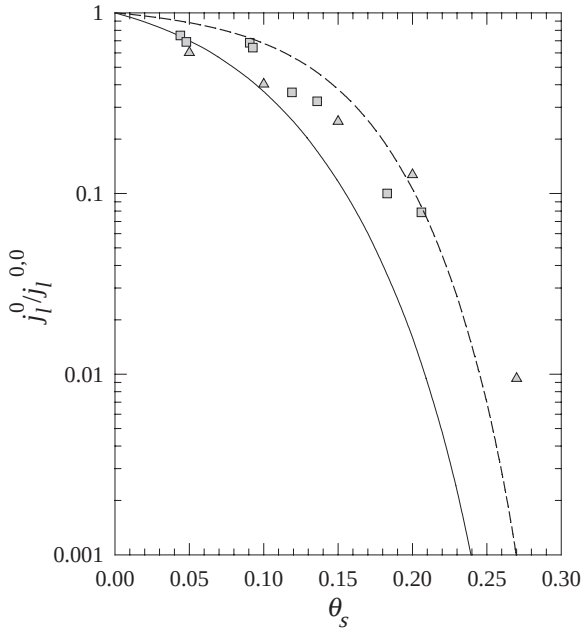

Fig. 21. Comparison of the theoretical and experimental, normalized initial adsorption flux, as a function of the small-particle surface coverage θ_s. Gray symbols (triangles and squares) depict two series of experiments. The solid and dashed lines denote results derived from the surface-force boundary-layer approximation (Eq. (41)) exploiting the $B_1^0(\theta_s)$ functions calculated numerically with the 2D and CT model, respectively Eq. (6). See more detail in text.

high. At high surface concentration, however, particle size polydispersity plays a significant role. As demonstrated in Ref. [26], assuming the constant particle diameter at a size polydispersity of 10% results in a 10% overestimation of the actual maximum surface coverage. Therefore one could expect that the actual θ_s is about 0.25; then the experimental result agrees well with theory.

On the contrary, the curve predicted by the 2D model and calculated for $K=2.5$, according to Refs. [31,40], underestimates the experimental results at $\theta_s>0.2$ by one order of magnitude and more, which results from overestimating of the blocking effect, as discussed above. A reasonably good agreement of the 2D model and the experimental results at the low surface coverage may be a consequence of the fact that in this regime, the overall transport rate is determined mostly by convective diffusion, due to a relatively small exclusion effect, and thus the inaccuracy introduced by the function B_1^0 is minor.

Fig. 22 presents the ASFs $B_1(\theta_1)$ computed for our model systems. The functions were calculated using the CT RSA model and the equilibrium equation (38) for the bimodal systems characterized by the parameters $\lambda=2$ and $\kappa a_1=8$ at four different values of the coverage: $\theta_s=0$ (reference curve), 0.02, 0.04, and 0.08. Based on the plots conclusions similar to these found in Fig. 20 can be drawn. As can be seen, both approaches give the same results within the limit of low surface coverage θ_s and θ_1. In the case of $\theta_s=0.08$, however, the difference between both curves is evident even at $\theta_1=0$. This difference results from the fact that the effective coverage corresponding to the system of the small particles is about 0.15, as can be estimated based on Fig. 16. In a similar way we can estimate the effective size and coverage corresponding to the other curves. Therefore, we conclude that electrostatic interaction can significantly increase blocking effects in bimodal systems, especially at small λ and high surface coverage, which becomes even more evident if we compare Figs. 21 and 3.

5.3.3. Maximum surface coverage

As with ASFs, the maximum surface coverage that determines monolayer capacity is of great practical interest. As demonstrated in a number of earlier studies, the quantity depends very much on ionic strength. However, quantitative estimations of the dependence, published in scientific papers, are not consistent and change with the model of adsorption used in simulations or with the experimental procedure. The results stemming from the 2D, 3D, and CT models are compared in Fig. 23. They were obtained for the parameter $\lambda=2$ at three values of the small-particle coverage: $\theta_s=0.02$, 0.04, and 0.08. As mentioned earlier, the computations were conducted for a few values of the parameter κa_1 and stopped after the dimensionless time $\tau=10^4$. The reported values of θ_{mx} correspond to that time.

At high ionic strength, corresponding to the large parameter κa_1, all the models predict the same values of the maximum coverage, in agreement with intuition. This is the

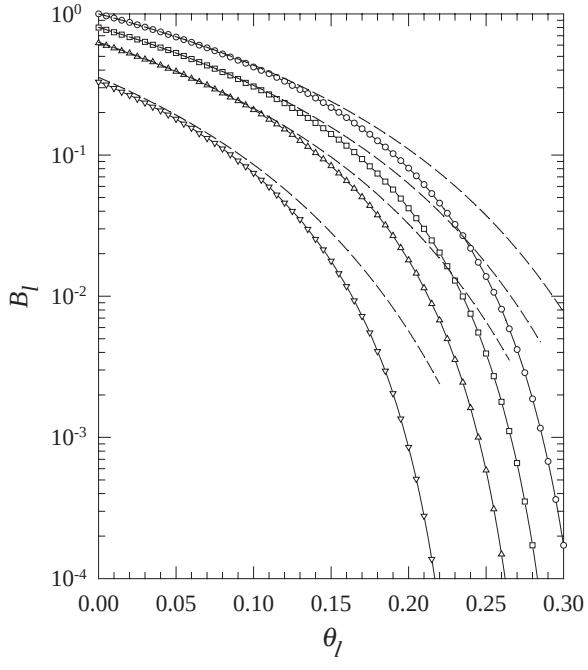

Fig. 22. Comparison of the ASF $B_1(\theta_1)$ calculated using the CT model (solid lines, Eq. (6)) and the equilibrium SPT (dashed lines, Eq. (38)) for the particle size ratio $\lambda=2$ and the parameter $\kappa a_1=8$. Open symbols denote different values of the small-particle surface coverage: $\theta_s=0$ (reference curve, circles), $\theta_s=0.02$ (squares), $\theta_s=0.04$ (triangles up), $\theta_s=0.08$ (triangles down).

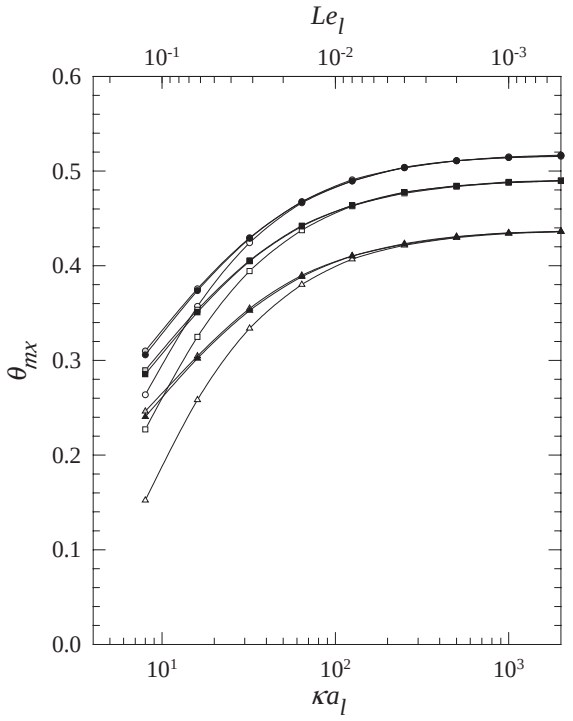

Fig. 23. Effect of the κa_1 parameter on the maximum surface coverage θ_{mx} predicted by three RSA models: 2D (open symbols), 3D (gray symbols), and CT (black symbols) at the particle size ratio $\lambda=2$. Circles, squares and triangles correspond to the small-particle surface coverage $\theta_s=0.02$, $\theta_s=0.04$, and $\theta_s=0.08$, respectively.

hard-particle limit that can be determined using the algorithm described in Section 2. At the range of the low κa_1 parameter, however, the results can be distinguished. Again, the plots obtained with the 3D and CT models are similar, whereas the 2D predicted results are much lower, which results from the overestimated blocking effects. Therefore, one can conclude that unlike the 2D model, the 3D model gives a reasonably good approximation of the maximum surface coverage at a lower computational cost, when compared to the CT model. The results are somewhat overestimated because of the assumption of the linear particle trajectory, which can result in slightly higher coverage θ_{mx}. The maximum coverage θ_{mx} decreases with ionic strength and with increase of the small-particle coverage θ_s.

The last conclusion can be drawn based on Fig. 24 as well. The results presented there were obtained using the CT model for two values of the coverage: $\theta_s=0.02$ and 0.08; and for three values of the parameter λ: 1, 2, and 4. As can be seen, in the presented range of κa_1 the effect of the parameter λ on the maximum surface coverage decreases with κa_1. The trend is consistent with the decrease of the effective particle size ratio λ^* at lower ionic strength, as described in Section 4. It is clear, however, that the lowering of the effective size ratio does not explain why the plotted curves cross over one another. Obviously, at high ionic strength, when the particles can be considered hard, the maximum coverage decreases with increase of λ, as discussed in Section 2. The opposite effect should be detectable at low ionic strength. It seems to result from the interplay between the particle–particle repulsion and the particle–interface attraction, as discussed above. At sufficiently low electrolyte concentrations the smaller particles, corresponding to the larger λ, allow more efficient interception of the large particle because of the "rolling" mechanism.

5.3.4. Pair-correlation function

Electrolyte ionic strength has a great impact not only on the kinetic aspects of large-particle adsorption but on controlling the formed monolayer structure as well. As was demonstrated above, lowering of the κa_i parameter results in a significant increase of the effective minimum particle surface-to-surface distance, which affects the pair-correlation function. In a real system, the function can be determined using experimental techniques. Therefore, by manipulating ionic strength we can easily verify a particle-deposition model in respect to both kinetics and structure. In actuality, the experimental determination of the correlation function is a difficult task because of the large number of particles needed to eliminate fluctuations and obtain a reasonably smooth curve. Moreover, some of the methods, like optical microscopy, have limited accuracy because of low image resolution, rarely exceeding few tens of pixels per particle diameter. As demonstrated in Ref. [34],

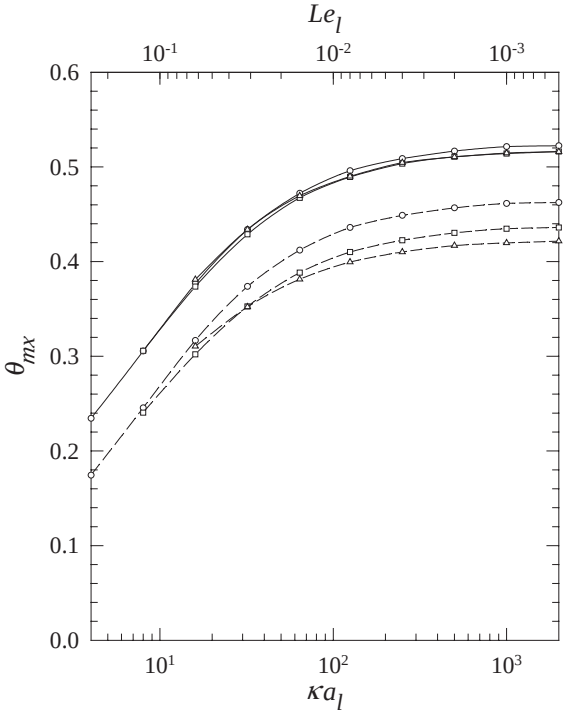

Fig. 24. Effect of the κa_1 parameter on the maximum surface coverage θ_{mx} predicted by the CT model for three values of the particle size ratio: $\lambda=1$ (circles), $\lambda=2$ (squares), and $\lambda=4$ (triangles). Solid and dashed lines denote results obtained at the small-particle surface coverage $\theta_s=0.02$ and $\theta_s=0.08$, respectively.

fluctuations present at such resolution are still large. The difficulties, however, are technical in nature and can be overcome with the further development of the experimental technique and electronics.

To begin with, Fig. 25 presents a comparison of the pair-correlation functions of the monodisperse system computed for the 2D, 3D, and CT models according to Eq. (3) for the following parameters: a_1=500 nm, κa_1=10, and θ_1=0.25. As can be seen, the primary peaks are located at r_p/a_1=2.9, 2.7, and 2.85, as predicted by the 2D, 3D, and CT models, respectively. The positions correspond well to the effective minimum particle surface-to-surface distances, as presented in Fig. 16, and are equal to 2.65, 2.5, and 2.7, respectively. Assuming that the effective hard-particle radius equals half of the effective minimum distance, $a_1^* = 0.5h_{11}^*$, all the peaks are located in the interval $r_p/a_1^* \in (2.1; 2.2)$, which agrees with the hard-particle result. The high maximum evident in the figure, obtained with the CT model, results from including the "rolling" effect into the model. In agreement with the algorithm and ASFs presented above, the correlation function computed with the 3D model is shifted toward the smaller interparticle distance, corresponding to the stronger lateral repulsion. At the particle–particle distance larger than three particle radii, both 3D and CT models give very similar results. All the three functions are basically indistinguishable at the distance larger than four radii, predicting the same position of the shallow minimum at r/a_1=4.8.

We computed the plots depicted in the next figure using the three models at the following parameters of the bimodal system: λ=4, κa_1=16, θ_s=0.08, and θ_1=0.146. The primary maxima obtained for higher ionic strength are located at the smaller distances r_p/a_1=2.45, 2.55, and 2.57 according to the 2D, 3D, and CT models, respectively. The corresponding effective minimum distances are equal to 2.42, 2.38, and 2.5 and comply with the peaks' position. The shift of the primary maximum toward the shorter interparticle distance as well as the appearance of the secondary peak of the correlation function demonstrates that the system computed with the 2D model is in the range of the high surface coverage, achieved at a relatively long adsorption time. Again, this effect is a consequence of the stronger blocking effects in the model, resulting in the lower maximum coverage. It should be noted that the secondary maximum is located just one particle radius from the primary maximum, which suggests that its

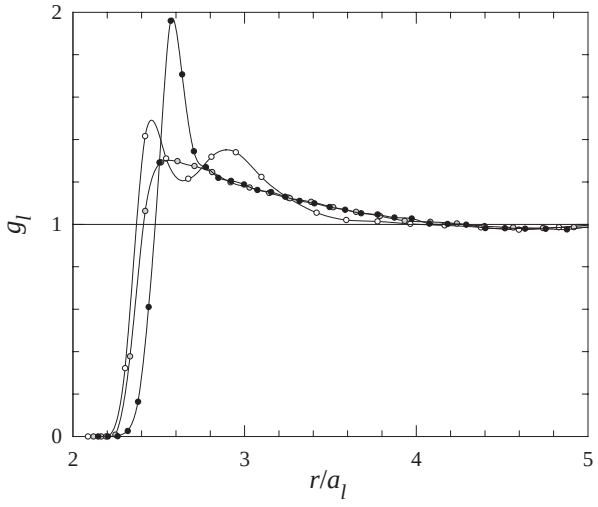

Fig. 26. Comparison of radial distribution functions $g_1(r/a_1)$ calculated using Eq. (3), based on the simulation data obtained with three RSA models: 2D (open circles), 3D (gray circles), and CT (black circles). The results refer to the bimodal system at the particle size ratio λ=4, small- and large-particle surface coverage θ_s=0.08 and θ_s=0.146, and the parameter κa_1=16.

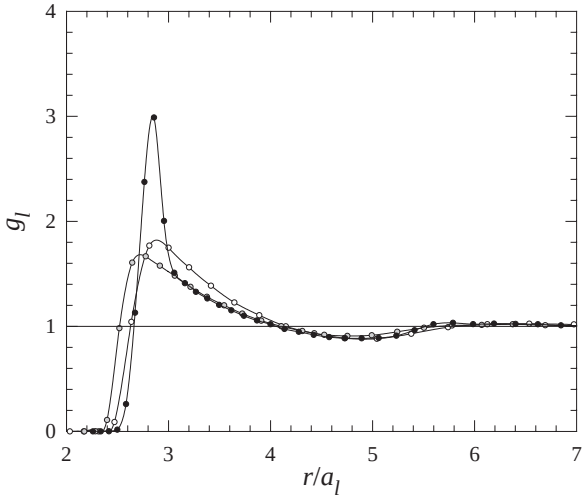

Fig. 25. Comparison of radial distribution functions $g_1(r/a_1)$ calculated using Eq. (3), based on the simulation data obtained with three RSA models: 2D (open circles), 3D (gray circles), and CT (black circles). The results refer to the monodisperse system (θ_s=0) at the parameter κa_1=10 and the large-particle surface coverage θ_s=0.25.

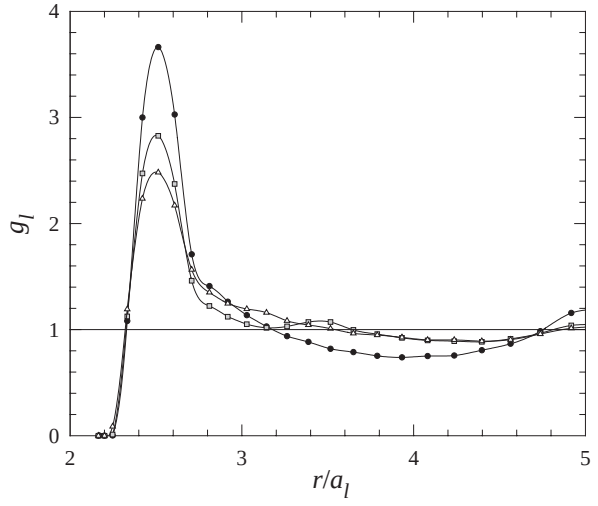

Fig. 27. Radial distribution functions $g_1(r/a_1)$ calculated using Eq. (3), based on the data derived from the CT simulations for the particle size ratio λ=1 (circles), λ=2 (squares), and λ=4 (triangles). The curves were computed at the small-particle surface coverage θ_s=0.08 and the parameter κa_1=16, close to jamming ($\tau = 10^4$).

appearance is caused by the presence of the small particles. As in the monodisperse system, the CT model predicts a relatively high and sharp primary maximum reflecting the "particle-rolling" effect. The 3D correlation function is shifted toward the smaller distance because it neglects that effect. The distance at which both functions can be considered identical is shorter than it was in case of the monodisperse systems and corresponds to the shorter effective minimum particle surface-to-surface distance at higher ionic strength (Fig. 26).

The pair-correlation functions appearing in Fig. 27 demonstrate the effect of particle size ratio as predicted by the model CT RSA at $\kappa a_1=16$, $\theta_s=0.08$, and $\theta_1=\theta_{mx}$. In agreement with intuition, the g_1 function maximum position at $r/a_1=2.5$ does not depend on λ and corresponds very well to the effective minimum particle distance. On the other hand, the peak height evidently decreases with an increase of the λ parameter. This effect can result from the fact that the tinier particles, more dispersed over the adsorption surface, cause larger irregularities in the large-particle structure. A very low secondary peak can be observed for $\lambda=2$ at the distance $r/a_1=3.5$, as can the heightened values of the correlation function corresponding to $\lambda=4$ at the distance $r/a_1=3$. As discussed above, the position of the deviations from the monodisperse functions suggests that their appearance is caused by the preadsorbed small particles. However, the correlation function obtained for $\lambda=1$, with the secondary maximum located at a distance two times larger than the primary one, seems to be indistinguishable from its monodisperse counterpart.

The effect of ionic strength on correlation functions is presented in Fig. 28. The functions were computed for the parameters $\lambda=4$, $\theta_s=0.08$, and $\theta_1=\theta_{mx}$ at three values of the parameter $\kappa a_1=16$, 32, and 64, using the CT model. The primary maxima are located at $r/a_1=2.5$, 2.3, and 2.15, respectively, and comply with the effective minimum distance depicted in Fig. 16. The peaks corresponding to the smaller parameter κa_1 are lower and more diffused, in agreement with intuition. The heightened values of the correlation functions to the right of the peaks suggest an effect caused by the smaller, preadsorbed particles. Based on the figure we may draw a more general conclusion that the presence of smaller particles at the adsorption surface can be manifested by an increase of the correlation function at the distance of about $r=r_{pp}+2d_{ls}^{*}$, where r_{pp} is the primary peak location. The effect becomes significant, however, at the higher coverage θ_1.

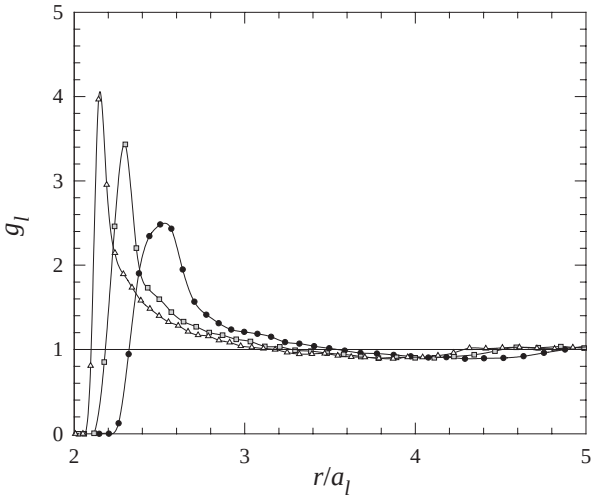

Fig. 28. Radial distribution functions $g_1(r/a_1)$ calculated using Eq. (3), based on the data derived from the CT simulations for the particle size ratio $\lambda=4$ at three values of the parameter $\kappa a_1=16$ (black circles), $\kappa a_1=32$ (gray squares), and $\kappa a_1=64$ (open triangles). The curves were computed at the small-particle surface coverage $\theta_s=0.08$, close to jamming ($\tau=10^4$).

6. Conclusion

The analysis of the extended RSA models and their results clearly suggests that these models are suitable for quantitative studies of adsorption on precovered surfaces in terms of the effective minimum particle surface-to-surface distance, ASF, correlation function, and maximum coverage. In connection with the surface-force boundary-layer approximation, the models allow determination of the adsorption kinetics as well.

Adsorption of colloid or nanoparticles at high ionic strength ($\kappa a_i>100$) can accurately be described by the hard-sphere RSA model, considering geometry-based particle overlapping only. At lower ionic strength, incorporating the electrostatic interaction into the model becomes necessary. The simplest version of the model allowing the soft interaction is the 2D RSA model, which assumes the PS particle–interface interaction and considers just the lateral particle–particle interaction. Consequently, this model overestimates the blocking effect and predicts the quasi-equilibrium pair-correlation function. Therefore, application of this model seems to be restricted to monodisperse systems and low surface coverage, as well as for systems where the particle-adsorption surface interaction is very short ranged. The more sophisticated model, 3D RSA, which considers the electrostatic interaction particle–interface, adequately describes the kinetic aspects of adsorption in the full range of the κa_i parameter ($\kappa a_i>4$). However, because the linear particle trajectory is assumed, this model does not predict the correct correlation function, especially at high surface coverage. It seems that at present the best tool for studying the kinetic and structural aspects of adsorption is the CT RSA model, which includes the electrostatic particle–interface interaction and considers the curvilinear particle trajectory at a relatively low computational cost. Depending on requirements, the model can be modified to include additional effects such as external forces or convection or Brownian motion.

Computation results suggest that minimal surface coverage by small particles can effectively block colloid deposi-

tion. The effect grows with the coverage θ_s and particle size ratio λ. Electrical interaction can enhance the effect, too, especially at the short interaction range ($\kappa a_i > 10$) with a small λ parameter, when the interparticle repulsion dominates over the particle–interface attraction. In the case of $\kappa a_i < 10$ and a large particle-size asymmetry, however, the computations suggest domination of the attraction to the adsorption surface, which can result in a diminishing of the blocking effect, even in comparison with hard-particle systems.

The presence of small particles at the adsorption surface can be detected not only by measuring the adsorption flux or the maximum coverage, but also by determining the large-particle radial correlation function, which becomes higher at the separation distance corresponding to two large particles with one small particle in between. In the case of the large coverage θ_l, a low secondary peak can even appear to the right of the primary maximum.

The application of the EHP concept allows extension of the SPT for bimodal systems of soft particles. The derived analytical formulae for the ASF are a good approximation of the numerical results in the range of low surface coverage.

Acknowledgements

The author thanks Prof. Z. Adamczyk for stimulating discussions, Dr. B. Siwek for providing the experimental results, and all co-workers of the Colloid Groups of the Institute of Catalysis and Surface Chemistry for creating a stimulating atmosphere. This work was partially supported by KBN Grant No. 3 T09A 089 27. Los Alamos National Laboratory technical support is also gratefully acknowledged.

References

[1] Boluk MY, van de Ven TGM. Colloids Surf 1990;46:157–76.
[2] van de Ven TGM, Kelemen SJ. J Colloid Interface Sci 1996;181:118–23.
[3] Adamczyk Z, Siwek B, Weroński P, Zembala M. Prog Colloid Polym Sci 1998;111:41–7.
[4] Hinrichsen EL, Feder J, Jossang T. J Stat Phys 1986;44:793–827.
[5] Schaaf P, Talbot J. J Chem Phys 1989;91:4401–9.
[6] Talbot J, Tarjus G, Schaaf P. Phys Rev, A 1989;40:4808–11.
[7] Viot P, Tarjus G. Europhys Lett 1990;13:295–300.
[8] Tarjus G, Viot P, Ricci SM, Talbot J. Mol Phys 1991;73:773–87.
[9] Viot P, Tarjus G, Ricci SM, Talbot J. J Chem Phys 1992;97:5212–8.
[10] Ricci SM, Talbot J, Tarjus G, Viot P. J Chem Phys 1992;97:5219–28.
[11] Adamczyk Z, Weroński P. J Chem Phys 1996;105:5562–73.
[12] Schaaf P, Johner A, Talbot J. Phys Rev Lett 1991;66:1603–5.
[13] Senger B, Voegel J-C, Schaaf P, Johner A, Schmitt A, Talbot J. Phys Rev, A 1991;44:6926–8.
[14] Senger B, Schaaf P, Voegel J-C, Johner A, Schmitt A, Talbot J. J Chem Phys 1992;97:3813–20.
[15] Senger B, Talbot J, Schaaf P, Schmitt A, Voegel J-C. Europhys Lett 1993;21:135–40.
[16] Jullien R, Meakin P. J Phys A 1992;25:L189–94.
[17] Choi HS, Talbot J, Tarjus G, Viot P. J Chem Phys 1993;99:9296–303.
[18] Tarjus G, Viot P, Choi HS, Talbot J. Phys Rev, E 1994;49:3239–52.
[19] Schaaf P, Wojtaszczyk P, Mann EK, Senger B, Voegel J-C, Bedeaux D. J Chem Phys 1995;102:5077–81.
[20] Adamczyk Z, Zembala M, Siwek B, Warszyński P. J Colloid Interface Sci 1990;140:123–37.
[21] Adamczyk Z, Weroński P. Langmuir 1995;11:4400–10.
[22] Adamczyk Z, Weroński P. J Colloid Interface Sci 1997;189:348–60.
[23] Oberholzer MR, Stankovich JM, Carnie SL, Chan DYC, Lenhoff AM. J Colloid Interface Sci 1997;194:138–53.
[24] Talbot J, Schaaf P. Phys Rev, A 1989;40:422–7.
[25] Meakin P, Jullien R. Phys Rev, A 1992;46:2029–38.
[26] Adamczyk Z, Siwek B, Zembala M, Weroński P. J Colloid Interface Sci 1997;185:236–44.
[27] Adamczyk Z, Siwek B, Weroński P. J Colloid Interface Sci 1997;195:261–3.
[28] Adamczyk Z, Weroński P. J Chem Phys 1998;108:9851–8.
[29] Adamczyk Z, Weroński P, Musiał E. J Chem Phys 2002;116:4665–72.
[30] Adamczyk Z, Weroński P, Musiał E. J Colloid Interface Sci 2002;248:67–75.
[31] Adamczyk Z. In: Toth J, editor. Irreversible adsorption of particles in adsorption: theory, modeling and analysis. New York: Marcel-Dekker; 2002. p. 251–374.
[32] Adamczyk Z, Weroński P, Musiał E. J Colloid Interface Sci 2001;241:63–70.
[33] Weroński P. Bull Pol Acad Chem 2003;51:221–39.
[34] Weroński P. Colloids Surf, A Physicochem Eng Asp (submitted for publication).
[35] Johnson CA, Lenhoff AM. J Colloid Interface Sci 1996;179:587–99.
[36] Adamczyk Z, Siwek B, Zembala M, Belouschek P. Adv Colloid Interface Sci 1994;48:151–280.
[37] Reiss H, Frisch HL, Lebowitz JL. J Chem Phys 1959;31:369–80.
[38] Widom B. J Chem Phys 1966;44:3888–94.
[39] Adamczyk Z, Senger B, Voegel J-C, Schaaf P. J Chem Phys 1999;110:3118–28.
[40] Adamczyk Z, Weroński P. Adv Colloid Interface Sci 1999;83:137–226.
[41] Lebowitz JL, Helfand E, Praestgaard E. J Chem Phys 1965;43:774–9.
[42] Talbot J, Jin X, Wang NHL. Langmuir 1994;10:1663–6.
[43] Evans JW. Rev Mod Phys 1993;65:1281–329.
[44] Bell GM, Levine S, McCartney LN. J Colloid Interface Sci 1970;33:335–59.
[45] Ohshima H, Healy TW, White LR. J Colloid Interface Sci 1982;90:17–26.
[46] Elimelech M, Gregory J, Jia X, Williams R. Particle deposition and aggregation: measurement, modelling and simulation. Oxford: Butterworth-Heinemann Ltd; 1995. p. 224–30.
[47] Zwanzig RW. J Chem Phys 1954;22:1420–6.
[48] McQuarrie DA, Katz JL. J Chem Phys 1966;44:2393–7.
[49] Rowlinson JS. Mol Phys 1964;7:349–61;
Rowlinson JS. Mol Phys 1964;8:107–15.
[50] Barker JA, Henderson D. J Chem Phys 1967;47:4714–21.
[51] Brenner SL. J Chem Phys 1976;80:1473–7.
[52] Minton AP, Edelhoch H. Biopolymers 1982;21:451–8.
[53] Piech M, Walz JY. Langmuir 2000;16:7895–9.
[54] Weroński P, Walz JY. J Colloid Interface Sci 2003;263:327–32.
[55] Adamczyk Z, Siwek B, Zembala M, Warszyński P. J Colloid Interface Sci 1989;130:578–87.
[56] Adamczyk Z, Warszyński P, Szyk-Warszyńska L, Weroński P. Colloids Surf, A Physicochem Eng Asp 2000;165:157–87.